

Updated constraints on velocity and momentum-dependent asymmetric dark matter

Aaron C. Vincent,^{1,2} Pat Scott² and Aldo Serenelli³

¹Institute for Particle Physics Phenomenology (IPPP), Department of Physics, Durham University, Durham DH1 3LE, UK

²Department of Physics, Imperial College London, Blackett Laboratory, Prince Consort Road, London SW7 2AZ, UK

³Institut de Ciències de l'Espai (ICE-CSIC/IEEC), Campus UAB, Carrer de Can Magrans s/n, 08193 Cerdanyola del Valls, Spain

E-mail: aaron.vincent@durham.ac.uk, p.scott@imperial.ac.uk, aldos@ice.csic.es

Abstract. We present updated constraints on dark matter models with momentum-dependent or velocity-dependent interactions with nuclei, based on direct detection and solar physics. We improve our previous treatment of energy transport in the solar interior by dark matter scattering, leading to significant changes in fits to many observables. Based on solar physics alone, DM with a spin-independent q^4 coupling provides the best fit to data, and a statistically satisfactory solution to the solar abundance problem. Once direct detection limits are accounted for however, the best solution is spin-dependent v^2 scattering with a reference cross-section of 10^{-35} cm^2 (at a reference velocity of $v_0 = 220 \text{ km s}^{-1}$), and a dark matter mass of about 5 GeV.

Contents

1	Introduction	1
2	Dark matter in the Sun	3
2.1	Capture in the Sun	3
2.2	Conductive energy transport by dark matter	5
3	Direct detection bounds	7
4	Solar bounds	9
4.1	Combined constraints	11
5	Conclusions	17
A	Contour plots of solar observables	18

1 Introduction

Despite tremendous success in predicting neutrino fluxes and describing the bulk structure of the Sun, the Standard Solar Model (SSM) still fails to reproduce key observables relating to helioseismology. After the downward revision of solar photospheric abundances over 10 years ago [1–12] it has become clear that the predicted sound speed profile, position of the base of the convection zone and surface helium abundance are all several standard deviations away from the values obtained by direct helioseismological inversion [13–18]. Despite over a decade of effort, no adequate solution has been found to reconcile solar modelling with these precision observables [19–22], prompting a search for solutions beyond the Standard Model.

As the Sun travels through the dark matter halo of the Milky Way, it inevitably interacts with the dark matter population¹. If a DM particle scatters with a nucleus in the Sun to a velocity less than the local escape velocity, it becomes gravitationally bound. From there, it will quickly settle into an equilibrium orbit near the solar centre, governed by the thermodynamics of the weakly-interacting DM gas in the steep gravitational potential of the Sun. The effects of dark matter capture in stars has been studied in depth since the 1980s [24–61]. In the absence of self-annihilation (i.e. asymmetric dark matter, ADM [62, 63]), a large population of dark matter can accumulate. This can act as a heat conductor, acquiring kinetic energy from the hot core, and releasing it via interactions with nuclei in the cooler outer regions. This can lead to a slightly shallower temperature gradient with height in the star. Despite the small population of DM (at most ~ 1 particle per 10^{10} baryons), these small adjustments in the thermal gradient can have measurable effects on our own Sun. These include the solar structure itself – including the sound speed $c_s(r)$ and convective zone radius r_{CZ} – and on neutrino fluxes from fusion processes, due to their strong dependence on the core temperature.

Precision solar models that include capture and heat transport from standard spin-dependent or spin-independent ADM can be built to satisfy the solar radius, age and luminosity [64–66]. Whilst these models can bring some helioseismological observables into

¹For a review of dark matter, see e.g. [23] and references therein.

better agreement with data than the SSM, this comes at the cost of an elastic scattering cross-section that is several orders of magnitude higher than allowed by direct detection experiments. These models also lead to drastic underproduction of solar neutrinos.

However, the kinetic regime probed by solar capture is very different from earth-based direct detection experiments: the Sun preferentially captures slower-moving particles from the DM halo, as these are more likely to scatter to sub-escape velocities, whereas direct detection relies on large enough velocities to produce observable recoils in a target material. This observation is partly what led to efforts to examine DM models with less trivial interactions with the Standard Model [67–71]. Such interactions are generic in particle physics: scattering mediated by a massive particle generally gives rise to non-relativistic elastic scattering cross section that is proportional to some positive power of the momentum transfer q or relative velocity v (see e.g. [72]). Conversely, new long-range forces can yield cross sections proportional to negative powers of these quantities (e.g. [73]).

Recently, we found [70, 71] that a light asymmetric particle with a momentum-dependent interaction with quarks could be captured in large enough quantities in the Sun and conduct heat in such a way that helioseismic observables could be brought into excellent agreement with data. Although this led to a reduction in the predicted neutrino fluxes, the significant improvement in sound speed and convective zone depth was sufficient to produce a marked improvement over the SSM of 6 standard deviations and a potential solution to the solar composition problem. New searches by direct detection experiments at low scattering threshold have since ruled out the best fit from these studies. CRESST-II [74] analysed the specific model highlighted in [70, 71] excluding it to high significance. The even more sensitive CDMSlite analysis [75] released by the SuperCDMS collaboration around the same period confirms this result.

We have furthermore revised the formalism of [67], and found that the conductive luminosity had been over (under) estimated in models with a cross section proportional to a positive (negative) power of q or v . We have corrected this error, finding that the best fit point in each model has moved in the parameter space. The best fits that we find are as good as those we found in [70, 71], though the required cross sections are higher, in some cases by as much as an order of magnitude. Given the strength of the direct detection bounds that we derive in this work, this is of little consequence as the previously-favoured parameter space is now entirely ruled out.

Our goals in this work are therefore 1) to update our solar simulations, correcting the error in luminosity, and 2) to confront these results with constraints from direct detection, to determine whether such models can indeed lead to a solution to the solar composition problem. We find that the parameter space that remains, after taking into account the recent CDMSlite results, is highly restricted. Although the models that obey these bounds do not fit the solar data as well as some that are excluded by direct detection, they are nonetheless capable of producing very significant improvements over the SSM (see also [69] for similar results).

This paper is structured as follows. In Sec. 2 we outline the class of models that we are considering, and present the relevant equations for capture by the Sun and heat transport within it. In Sec. 3 we briefly discuss constraints from direct detection on light DM particles able to affect solar structure. We present the results of our simulations in Sec. 4, and conclude in Sec. 5.

2 Dark matter in the Sun

The method of obtaining the capture rate and subsequent energy transport due to momentum or velocity-dependent DM in the Sun is presented in detail in Refs. [67, 71]. Here, we show the main results, along with a crucial correction to the transported luminosity formula, Eq. 2.12. Reflecting the nature of most concrete models so far proposed in the theory literature, we focus on models with isoscalar (identical proton and neutron) DM-nucleon couplings with the Standard Model. We parameterise the resulting differential cross-sections as

$$\sigma = \sigma_0 \left(\frac{q}{q_0} \right)^{2n} \quad (2.1a) \quad \text{and} \quad \sigma = \sigma_0 \left(\frac{v_{\text{rel}}}{v_0} \right)^{2n}. \quad (2.1b)$$

Each of these can be spin-independent (SI), coupling coherently to all nucleons; or spin-dependent (SD), coupling only to the spin of unpaired nucleons. This “form factor” approach [76], encompasses both non-relativistic effective operators that can come from effective point-like interactions [77–79], as well as certain classes of long-range forces (e.g. [73]). The cross section for scattering with a nucleus is then

$$\sigma_{N,i} = \frac{m_{\text{nuc}}^2 (m_\chi + m_p)^2}{m_p^2 (m_\chi + m_{\text{nuc}})^2} \left[\sigma_{\text{SI}} A_i^2 + \sigma_{\text{SD}} \frac{4(J_i + 1)}{3J_i} |\langle S_{p,i} \rangle + \langle S_{n,i} \rangle|^2 \right]. \quad (2.2)$$

2.1 Capture in the Sun

In the absence of annihilation or evaporation, the population of DM in the Sun is simply given by $\dot{N}_\chi(t) = C_\odot(t)$:

$$C_\odot(t) = 4\pi \int_0^{R_\odot} r^2 \int_0^\infty \frac{f_\odot(u)}{u} w \Omega(w) du dr. \quad (2.3)$$

Here, $f_\odot(u)$ is the DM speed distribution in the Sun’s frame, and $\Omega(w)$ encodes the kinematics of scattering below the local escape velocity $v_{\text{esc}}(r)$. $w(r) \equiv \sqrt{u^2 + v_{\text{esc}}^2}$ is the local DM velocity inside the star’s gravitational potential. Expressing the DM-to-nucleon mass ratio as $\mu_i \equiv m_\chi/m_{N_i}$, this quantity is:

$$\Omega(w) = \frac{2}{m_\chi w} \sum_i \sigma_{N,i} n_i(r, t) \frac{\mu_{i,+}^2}{\mu_i} \Theta \left(\frac{\mu_i v_{\text{esc}}^2}{\mu_{i,-}^2} - u^2 \right) GFFI(\mu, u, v_{\text{esc}}), \quad (2.4)$$

where $GFFI$ is the generalized form factor integral, and $n_i(r)$ is the number density of each nuclear species in the Sun. In the case of a constant cross section, the $GFFI$ is simply an integral over the nuclear form factor $F_i(E_R)$:

$$GFFI_{n=0} = \int_{m_\chi u^2/2}^{m_\chi w^2 \mu_i/2 \mu_{i,+}^2} |F_i(E_R)|^2 dE_R, \quad (2.5)$$

where the integral limits are set by the kinematics required to downscatter the DM velocity enough for it to be captured.

For velocity-dependent scattering, the required modification of the capture rate is straightforward: the integrand in Eq. 2.3 is simply multiplied by an overall factor of $[w(r)/v_0]^{2n}$.

When the cross section is momentum-dependent, the factors of $(q/q_0)^{2n}$ must be included inside the $GFFI$. For scattering with hydrogen (assuming a point-like particle, i.e.

$F_1(E_R) = 1$):

$$GFFI_{n \neq 0, H} = \left(\frac{p}{q_0}\right)^{2n} \frac{m_\chi w^2}{2\mu^n} \begin{cases} \frac{1}{1+n} \left[\left(\frac{\mu}{\mu_+^2}\right)^{n+1} - \left(\frac{u^2}{w^2}\right)^{n+1} \right], & (n \neq -1) \\ \ln\left(\frac{\mu}{\mu_+^2} \frac{w^2}{u^2}\right), & (n = -1) \end{cases} \quad (2.6)$$

where $p = m_\chi w$. For heavier nuclei, a parameterisation of the form factor must be chosen. Significant work over the past few years has gone into computing accurate form factors that model the nuclear response function using effective field theory; these yield interactions close to those in Eqs. 2.1 and Ref. [80] has computed these response functions for capture in the Sun. The standard Helm [81] parameterisation is

$$|F_i(E_R)|^2 = \exp\left(-\frac{E_R}{E_i}\right), \quad (2.7)$$

where E_i is a constant quantity for each nuclear species i , given by

$$E_i = \frac{5.8407 \times 10^{-2}}{m_{N,i}(0.91m_{N,i}^{1/3} + 0.3)^2} \text{GeV}. \quad (2.8)$$

For spin-independent capture and transport, we use the following 15 elements: H, He, C, N, O, Ne, Mg, Na, Al, Si, S, Ar, Ca, Fe and Ni. Though heavier elements are suppressed in abundance, the A^2 coherence factor in Eq. 2.2 can enhance the capture rate off these elements by as much as four orders of magnitude.

We have furthermore checked in Ref. [71] that for most models, the deviations with respect to Helm are minimal, as low-momentum scattering tends to dominate the capture rate. There is one exception: when computing spin-dependent capture rates, we neglect elements heavier than hydrogen. These do not benefit from the A^2 coherent enhancement present for spin-independent interactions, and their very low abundance further suppresses their contribution. However, in the q^4 SD case, which can be matched to an $\mathcal{O}_6 \equiv (\vec{S}_\chi \cdot \vec{q}/m_N)(\vec{S}_N \cdot \vec{q}/m_N)$ coupling, the total capture rate in an evolved solar model is actually dominated by scattering with nitrogen. This does not turn out to be very helpful, as we will find that the cross-section required to produce an effect in the Sun with this operator is ruled out by five orders of magnitude. We thus use the Helm form factor for every case, and the generalised form factor integral for momentum-dependent interactions becomes:

$$GFFI_{n \neq 0, i \neq H} = \left(\frac{p}{q_0}\right)^{2n} \frac{E_i}{(B\mu)^n} \left[\Gamma\left(1+n, B\frac{u^2}{w^2}\right) - \Gamma\left(1+n, B\frac{\mu}{\mu_+^2}\right) \right], \quad (2.9)$$

where $B \equiv \frac{1}{2}m_\chi w^2/E_i$, and $\Gamma(m, x)$ is the (upper) incomplete gamma function.

The Sun cannot capture more dark matter than the so-called geometric limit, in which all of the DM that intercepts the solar disk is captured. The total capture rate is therefore the smallest of Eq. 2.3 and

$$\begin{aligned} C_{\max}(t) &= \pi R_\odot^2(t) \int_0^\infty \frac{f_\odot(u)}{u} w^2(u, R_\odot) du \\ &= \frac{1}{3} \pi \frac{\rho_\chi}{m_\chi} R_\odot^2(t) \left(e^{-\frac{3}{2} \frac{u_\odot^2}{u_0^2}} \sqrt{\frac{6}{\pi}} u_0 + \frac{6G_N M_\odot + R_\odot(u_0^2 + 3u_\odot^2)}{R_\odot u_\odot} \text{Erf}\left[\sqrt{\frac{3}{2}} \frac{u_\odot}{u_0}\right] \right), \end{aligned} \quad (2.10)$$

where $u_0 = 270 \text{ km s}^{-1}$ is the dispersion of the Maxwell-Boltzmann DM velocity distribution, $u_\odot = 220 \text{ km s}^{-1}$ is the velocity of the Sun relative to the DM halo, and $\rho_\chi = 0.38 \text{ GeV cm}^{-3}$ is the local density of dark matter. We show the cross section that saturates this bound in Fig. 1, for each of the models we consider in this paper. Strictly speaking, the transition from Eq. 2.3 to 2.10 should be smooth, rather than a sharp cutoff as we impose here. To accurately model this transition, the full optical depth must be including in Eq. 2.3. This leads to a suppression of the capture rate as σ_0 approaches the saturation cross section, with the ultimate effect of slightly suppressing the effect of DM close to this threshold. As this computation is relatively involved, we address it in an upcoming work [82].

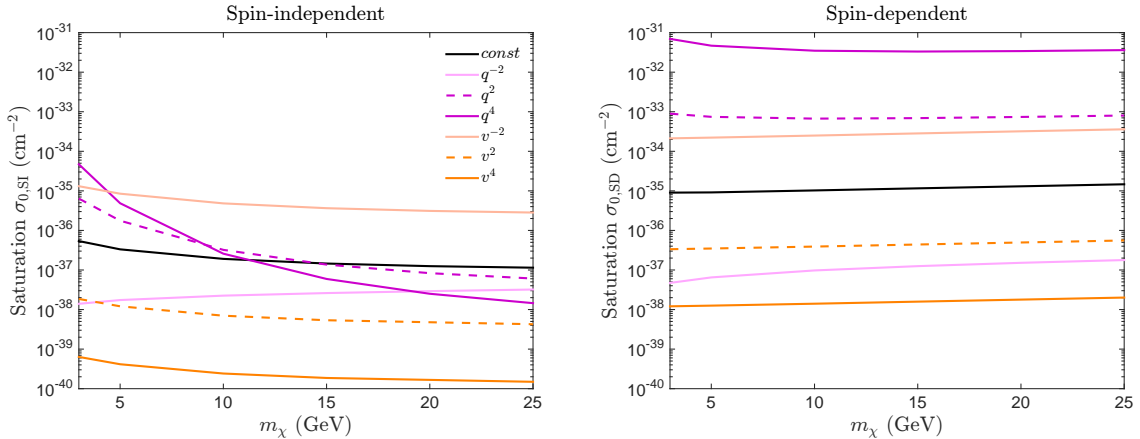


Figure 1. Cross section at which the capture rate computed in DarkStec saturates the geometric limit 2.10. Left: spin-independent interactions, coupling to every element; right: spin-dependent interactions with hydrogen only. Despite their small abundances, heavier elements contribute significantly to spin-independent capture, thanks in large part to the coherent $\sigma_N \propto A^2$ enhancement.

2.2 Conductive energy transport by dark matter

In the local thermal equilibrium (LTE) regime, where the mean DM interscattering distance l_χ is much smaller than the scale of the DM distribution r_χ , the equilibrium distribution of DM particles in the gravitational potential $\phi(r)$ of the Sun is given by [55, 67, 83]

$$n_{\chi,\text{LTE}}(r) = n_{\chi,\text{LTE}}(0) \left[\frac{T(r)}{T(0)} \right]^{3/2} \exp \left[- \int_0^r dr' \frac{k_B \alpha(r') \frac{dT(r')}{dr'} + m_\chi \frac{d\phi(r')}{dr'}}{k_B T(r')} \right], \quad (2.11)$$

where $r = 0$ represents the centre of the Sun. The conductive luminosity is:

$$L_{\chi,\text{LTE}}(r) = 4\pi r^2 \kappa(r) n_{\chi,\text{LTE}}(r) l_\chi(r) \left[\frac{k_B T(r)}{m_\chi} \right]^{1/2} k_B \frac{dT(r)}{dr}, \quad (2.12)$$

where we have removed the erroneous factor ζ^{2n} which was present in [67, 71]. Below, we will find that this has the effect of displacing the best fit regions in parameter space, to higher (lower) values of σ_0 for positive (negative) values of n . $v_T(r) \equiv \sqrt{2k_B T(r)/m_\chi}$ is related to the typical thermal velocity [83]; v_0 and q_0 are respectively the reference velocity and momentum defined in Eq. 2.1. The effect of our correction to Eq. 2.12 is to suppress

transport by models with positive powers of q and v , and enhance it for negative powers. The rate of energy transported per unit mass of stellar material is:

$$\epsilon_{\chi,\text{LTE}}(r) = \frac{1}{4\pi r^2 \rho(r)} \frac{dL_{\chi,\text{LTE}}(r)}{dr}. \quad (2.13)$$

This quantity is usually expressed in units of $\text{erg g}^{-1} \text{s}^{-1}$. The molecular diffusion coefficient $\alpha(r, \mu)$ and conduction coefficient $\kappa(r, \mu)$ are computed by perturbatively solving a Boltzmann collision equation in the diffuse gas limit. This method was introduced by Gould and Raffelt [83] and generalised in Ref. [67]; as before, we use the tabulated coefficients given in the latter reference.

In the non-LTE, ‘‘Knudsen’’ regime $K \equiv l_{\chi}/r_{\chi} \gg 1$, the DM distribution becomes isothermal:

$$n_{\chi,\text{iso}}(r, t) = N(t) \pi^{-3/2} r_{\chi}^{-3} \exp(-r^2/r_{\chi}^2), \quad (2.14)$$

Gould and Raffelt [83] found that the transition to the LTE regime could be well described by the interpolating functions [55, 84]:

$$\mathfrak{h}(r) = 1 + \left(\frac{r - r_{\chi}}{r_{\chi}}\right)^3 \quad \mathfrak{f}(K) = \left[1 + \left(\frac{K}{K_0}\right)^{1/\tau}\right]^{-1}, \quad (2.15)$$

such that

$$n_{\chi}(r) = \mathfrak{f}(K)n_{\chi,\text{LTE}} + [1 - \mathfrak{f}(K)]n_{\chi,\text{iso}}, \quad (2.16)$$

and

$$L_{\chi,\text{total}}(r, t) = \mathfrak{f}(K)\mathfrak{h}(r, t)L_{\chi,\text{LTE}}(r, t). \quad (2.17)$$

Energy transport has the opposite behaviour as a function of the interaction cross section in the LTE and Knudsen regimes. In the LTE regime (large σ_0), a higher scattering rate suppresses the typical distance travelled, confining DM and suppressing energy transport. Conversely, in the Knudsen (small σ_0) regime, the inter-scattering distance is already large, and energy transfer is instead dominated by the collisional efficiency: luminosity thus increases with increasing cross section. Heat conduction is therefore maximised at the boundary between these regimes, when inter-scattering distances are large, but interaction rates are still large enough to allow efficient energy transfer. We show this behaviour in Fig. 2. It follows that the largest effect of momentum or velocity-dependent dark matter on solar observables will occur when the cross-section is closely matched to the Knudsen peak (as long as a sufficient amount of DM can be captured with this cross section).

In Fig. 3 we show the equivalent for the impact of DM mass, illustrating the strong enhancement of energy transport at low masses due to mass-matching between DM and hydrogen or helium. This corresponds to transitions in α and κ at $m_{\chi} \sim m_N$ for different interactions [67], and can also be seen in the fact that transport is maximised at lower masses for SD scattering, reflecting the fact that H plays a role due to its spin, but He does not. The combination of this effect with the transition from LTE to non-local transport can be seen in Fig. 4. Whilst this figure shows contours for momentum and velocity-independent scattering only, other interactions lead to a very similar pattern, just scaled or shifted in the x , y and/or z directions.

Finally, as the DM mass is lowered below 5 GeV, it may pick up sufficient speed from thermal collisions to escape the sun. This can lead to significant loss through evaporation.

However, the exact amount of evaporation depends sensitively on the mass and cross section. Since this dependence is not known, we also explore this region of the parameter space. In an upcoming work [82] we aim to compute these precise evaporation masses, for every model explored here.

3 Direct detection bounds

Recently, the SuperCDMS collaboration has presented their lowest-threshold analysis ever, [75]. This 70 kg day run was sensitive to recoil energies above 56 eVee (or around 300 eV nuclear recoil energies), allowing them to set exclusion bounds on DM masses extending below 2 GeV. Though CRESST-II [74] have presented analyses of specific models in this work, we use CDMSlite data because it is both more sensitive and easier to recast into new limits. Since CDMS uses a germanium crystal target, it presents the further advantage of being sensitive to spin-dependent interactions: 7.6% of natural Ge is in the form of ^{73}Ge ($J = 9/2$), allowing spin-dependent bounds to be derived with the same data set. In contrast, the CaWO_4 target used by CRESST-II presents no appreciable target mass with nonzero spin.

Assuming different SI and SD couplings, but equal couplings to protons and neutrons for each type of interaction (i.e. isoscalar couplings), the differential nuclear recoil rate is

$$\frac{dR}{dE_R} = \frac{\rho_\chi}{2m_\chi\mu_p} \int_{v_{\min}}^{\infty} \frac{f(v)}{v} \left(\sigma_{SI,p}(q, v) A^2 F_{SI}^2(E_R) + \sigma_{SD,p}(q, v) \frac{4(J+1)}{3J} [\langle S_n \rangle + \langle S_p \rangle]^2 F_{SD}^2(E_R) \right) dv, \quad (3.1)$$

where $\mu_p \sim \mu_n$ is the DM-nucleon reduced mass and $v_{\min} \equiv \sqrt{m_N E_R / 2\mu_N^2}$ is the minimum DM velocity required to produce a recoil with energy E_R . In this expression, μ_N is the DM-nucleus reduced mass. Using the binned data, efficiency curve and ionisation yield presented in Ref. [75] and a simple Poisson analysis, along with the same halo parameters as in our solar analysis, we obtain the exclusion curves presented in Fig. 5. For SI limits (left panel) we use the same form factor as for solar capture. For the spin-dependent limits (right panel), we assume scattering only on 7.6% of the target, and use the spin expectations and isoscalar structure function S_{00} from Ref. [85], such that

$$\frac{4(J+1)}{3J} [\langle S_n \rangle + \langle S_p \rangle]^2 F_{SD}^2(E_R) = \frac{16\pi}{3(2J+1)} S_{00}(E_R). \quad (3.2)$$

Although we show limits for isoscalar couplings only, it is worth noting that most of the unpaired spin contribution from ^{73}Ge comes from neutrons, so limits on ADM that couples mainly to protons would be significantly weaker. The SI limits in Fig. 5 are slightly more constraining than the limits presented by CRESST-II [74], for the spin-independent q^2 and q^4 cases.

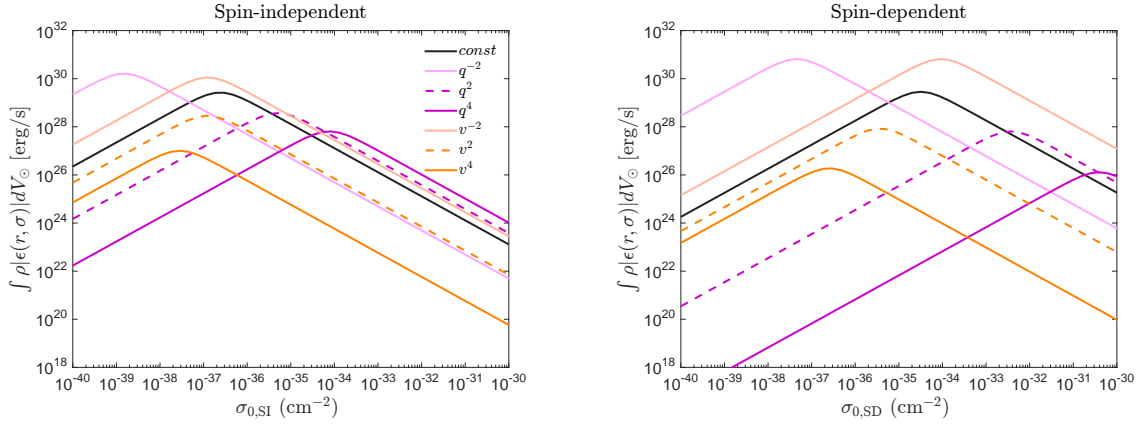


Figure 2. The transition from local thermal equilibrium (LTE) to the non-local, isothermal regime of energy transport by spin-independent (*left*) and spin-dependent DM scattering (*right*). Left of the peaks is the non-local regime, rightwards is the LTE regime. The total energy transport is plotted for a fixed DM mass ($m_\chi = 10$ GeV) and number ratio of DM to baryons ($n_\chi/n_b = 10^{-15}$).

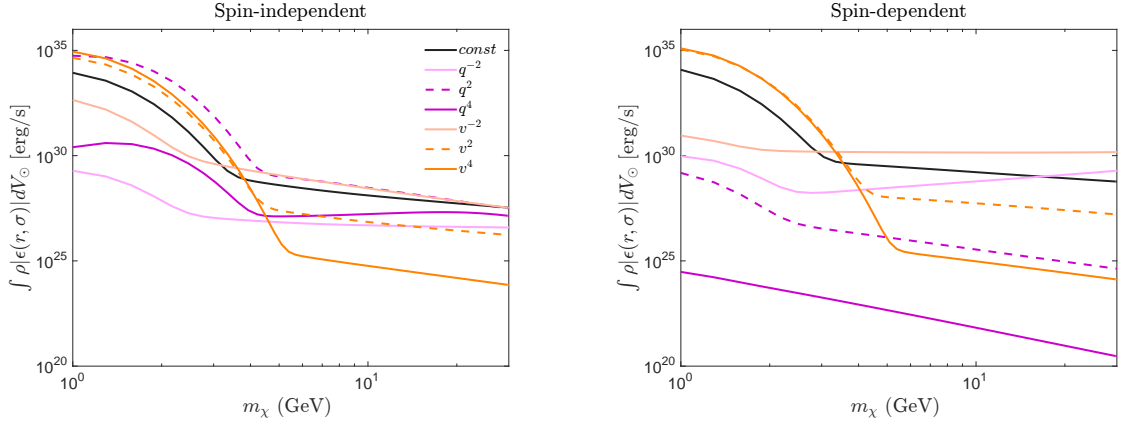


Figure 3. Mass dependence of energy transport by spin-independent (*left*) and spin-dependent DM scattering (*right*), for a fixed scattering cross-section ($\sigma_0 = 10^{-35}$ cm²) and number ratio of DM to baryons ($n_\chi/n_b = 10^{-15}$). Peaks are where DM is relatively closely matched in mass to H and/or He.

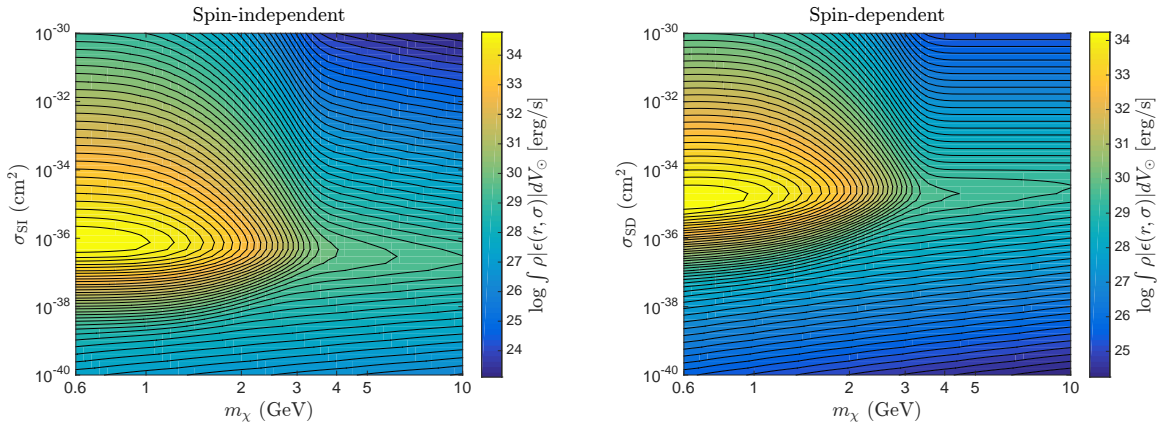


Figure 4. Joint dependence on cross-section and mass of energy transport by q - and v -independent interactions, assuming a fixed number ratio of DM to baryons ($n_\chi/n_b = 10^{-15}$).

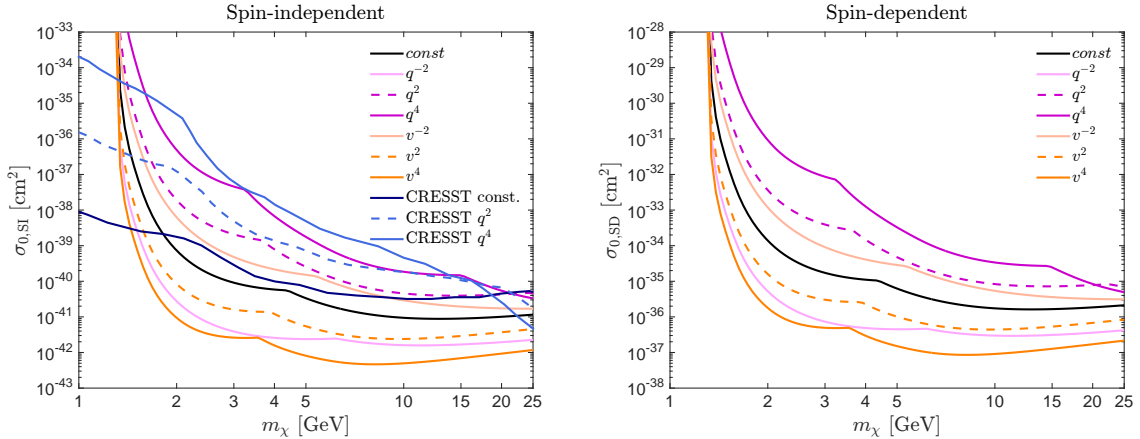


Figure 5. CDMSlite upper limits on σ_0 for the models that we consider, from the event rates and instrument details given in Ref. [75]. To compare with our Solar results, we use the same values of $v_0 = 220$ km/s and $q_0 = 40$ MeV. We also show results obtained by the CRESST-II low-threshold analysis taken from [74], which are slightly less constraining than CDMSlite for DM masses above 1.4 GeV.

4 Solar bounds

To produce our updated constraints, we employ the DarkStec code, developed for and described in Ref. [71]. DarkStec is a combination of the legendary GARSTEC solar evolution code [86, 87], and the lightweight capture and transport routines from DarkStars [52, 55, 88]. These were modified to include the full capture and transport technology described above, for momentum and velocity dependent dark matter. To obtain our results, we perform a scan over a grid of masses $m_\chi = \{3, 5, 10, 15, 20, 25\}$ GeV and one cross section per decade from $\sigma_0 = 10^{-40}$ to 10^{-30} cm², totalling over 900 simulations, or approximately 2.5 CPU years.

A full description of the observables that we use is given in Ref. [71]. Here we summarise the salient points. Solar neutrino fluxes and small frequency separations are highly sensitive to the impacts of DM on the core of the Sun, and typically provide the strongest constraints on DM models. The depth of the convection zone is sensitive to impacts of DM on the temperature gradient closer to the surface, and generally depends more subtly on the overall diffusivity of DM in the Sun. The surface helium abundance and radial profile of the sound speed profile probe the entire radiative region, but contribute comparatively little additional constraining power over other observables.

Plots of the neutrino fluxes, depth of the convection zone, sound-speed and small-separation likelihoods vs m_χ and σ_0 are presented in Appendix A. We also provide the full results of all our simulations, including each of these observables, their likelihoods and the combined likelihood presented in Sec. 4.1, as machine-readable supplementary material.

Our reference SSM uses the AGSS09 photospheric abundances [9].

Solar neutrino fluxes: Minute changes in the core temperature can have substantial effects on the solar neutrino fluxes, due to their steep temperature-dependence. The main fusion process in the Sun, $p + p \rightarrow {}^2\text{H} + e^+ + \nu_e$, is quite insensitive to changes due to DM energy transport, as the luminosity condition enforces a fairly constant reaction rate. However, the subdominant flux of neutrinos from the decay of ${}^8\text{B}$ produced in the

pp and pep chains is an especially good probe of the core temperature, as are the two lines at $E_\nu = 862$ keV and 384 keV from the decay of ${}^7\text{Be}$. While these are measured at 3% and 5% accuracy, respectively, the uncertainties in their production rates are closer to 14% and 7%. We add these errors in quadrature when assessing the goodness of fit. As the SSM is in very good agreement with the measured neutrino fluxes, this serves as a constraint on the total effect DM can have in the solar core. The changes in neutrino fluxes in different models are shown in Figs. 10-13. When uncertainties are compared on the same footing, our constant, SD results are in agreement with [64].

Depth of the convection zone: The radius at which hydrostatic equilibrium breaks down, radiative pressure is no longer balanced by gravity, and convective energy transport begins, depends crucially on the radial temperature and pressure gradients. The height of the convection zone can be inferred from helioseismological measurements, $R_{\text{CZ},\odot} = 0.713 \pm 0.001 R_\odot$, while the SSM predicts a much higher value: $R_{\text{CZ,SSM}} = 0.722 \pm 0.004 R_\odot$. As DM deposits energy at larger radii, the absolute temperature gradient increases slightly, thus lowering the location of the base of the convection zone. This is shown in Figs 14 and 15.

Surface helium abundance: As the initial mass fractions of hydrogen, helium and metals cannot be directly measured, they (along with the mixing length parameter α_{MLT}) are allowed to vary as DarkStec attempts to find a solution for the input parameters. The present-day surface helium abundance is thus predicted by these parameters, when combined with the physics entering into the SSM. The measured value is $Y_s = 0.2485 \pm 0.0034$, while the SSM yields $Y_s = 0.2356 \pm 0.0035$. The surface helium abundance essentially reflects the initial helium abundance, which is strongly constrained by the requirement that the model must reproduce the observed solar luminosity. Any change in initial helium abundance must come with a corresponding change in the initial hydrogen fraction, which modifies the resulting solar luminosity unless the core temperature is also drastically altered. In extreme cases, DM can have enough of an effect on the core temperature to change the resulting surface helium abundance expressed by a model – so we do include this observable in our fits – but typically, the effects on the core temperature are not drastic enough for this observable to be significantly affected.

Sound speed: The radial sound speed profile can be inferred by inverting the oscillation frequencies of the different angular modes projected onto the solar surface. Fig. 6 shows the sound speed profile obtained with our SSM (blue solid line), when compared with the errors from helioseismological measurement and inversions (green regions) and modelling (blue regions). The change in the temperature, pressure and density due to the redistribution of heat by DM can be quite large – as long as the cross section is large enough to saturate the capture rate and hit the Knudsen transition. Fig. 6 also shows the effect of three models which are allowed by DD constraints, along with one which is not (SI, q^4 , solid magenta line), but which illustrates the strong effect DM can have. We also show in Figs. 16 and 17 the goodness of fit of each of our models to the sound speed profile from helioseismology observations with SoHO and BiSON [89], using a chi-squared with 5 equally-spaced points between $R = 0.1R_\odot$ and $0.67R_\odot$, where helioseismic errors are minimal. Given the large modelling errors, however, and

the fact that c_s is highly correlated with the more precise frequency separation ratios, we do not include the sound speed in our total χ^2 .

Frequency separation ratios: It is possible to remove a large fraction of the systematic errors that enter sound speed inversions near the core by directly using specific combination of frequencies. Two most commonly used quantities are the so-called small frequency separation ratios [90]:

$$r_{02}(n) = \frac{d_{02}(n)}{\Delta_1(n)}, \quad r_{13}(n) = \frac{d_{13}(n)}{\Delta_0(n+1)}, \quad (4.1)$$

where $\Delta_l(n) \equiv \nu_{n,l} - \nu_{n-1,l}$ and

$$d_{l,l+2}(n) \equiv \nu_{n,l} - \nu_{n-1,l+2} \simeq -(4l+6) \frac{\Delta_l(n)}{4\pi^2 \nu_{n,l}} \int_0^{R_\odot} \frac{dc_s}{dr} \frac{dr}{r}. \quad (4.2)$$

These have the additional advantage of being insensitive to details in the structure of the external layers of the Sun, which are not properly modeled in SSMs. The $1/r$ dependence ensures sensitivity to the properties of the solar core, and the modeling and observational uncertainties on r_{02} and r_{13} are much smaller than for Solar neutrinos. These frequency separation ratios are shown in Fig. 7 for the SSM (red), and several models including energy transport by ADM.

4.1 Combined constraints

We define a combined chi-squared, including all of the quantities listed above except the sound speed profile:

$$\chi^2 = \frac{(1 - \phi_{\text{B,obs}}^\nu / \phi_{\text{B}}^\nu)^2}{\sigma_{\text{B}}^2} + \frac{(1 - \phi_{\text{Be,obs}}^\nu / \phi_{\text{Be}}^\nu)^2}{\sigma_{\text{Be}}^2} + \frac{(r_{\text{CZ}} - r_{\text{CZ,obs}})^2}{\sigma_{\text{CZ}}^2} + \frac{(Y_{\text{S}} - Y_{\text{S,obs}})^2}{\sigma_{Y_{\text{S}}}^2} + \chi_{r_{02}}^2 + \chi_{r_{13}}^2, \quad (4.3)$$

where ϕ_{B}^ν and ϕ_{Be}^ν correspond to the boron-8 and beryllium-7 neutrino fluxes, r_{CZ} is the depth of the convection zone, Y_{S} is the surface helium abundance, and r_{ij} are the small frequency separation ratios. The sound speed profiles are strongly correlated with the small separations, and less precise, so we do not use them. The subscript ‘‘obs’’ indicates the observed value. The errors σ_i include both modelling and observational error, added in quadrature.

The results of these combined constraints are given in Fig. 8 for spin-independent couplings, and Fig. 9 in the spin-dependent case. The thick magenta lines in these figures are the constraints that we obtained above from the latest CDMSlite data. There is very little parameter space in which DM is unconstrained by direct detection, yet has a strong enough effect on the Sun to change the fit.

The best-fit points for each model are given in Table 1. In all cases, the SI direct detection limits are too strong to allow any of our best-fit points. In only two spin-dependent cases (v^2 and v^4) are the best-fit points below the CDMSlite limits. In one other case (SD q^{-2}), there is a region that is almost as good as the best fit; we list this point instead. These allowed models are labelled with a dagger (\dagger) in Table 1.

Despite the low p-values, each of the allowed models still represents a remarkable improvement over the SSM. This improvement is driven by the much better fits to the small

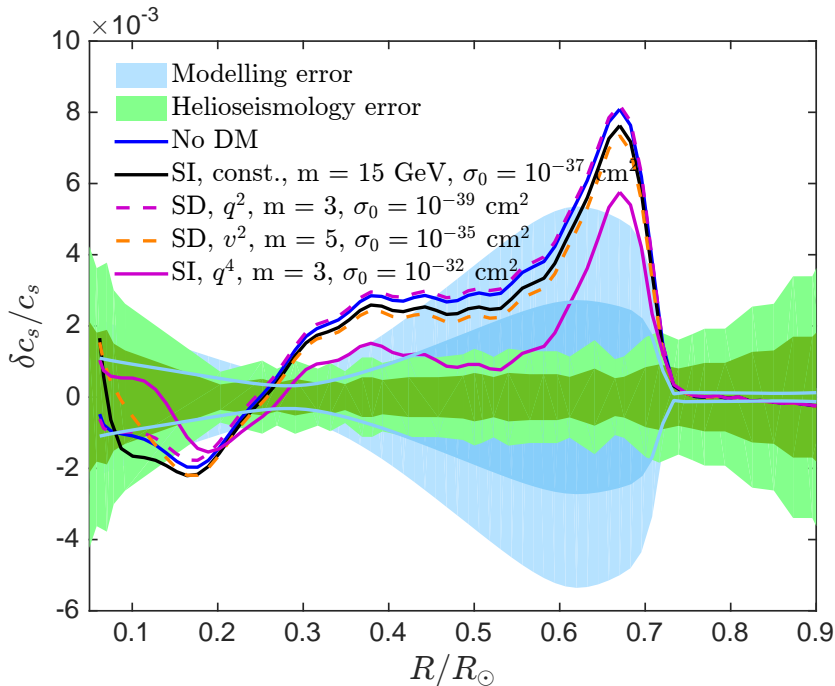


Figure 6. Deviation of radial sound speed profile from values inferred from combined SoHO and BiSON helioseismology data [89] using our SSM. We show the best fit for a constant cross section in black, and the two best fits that are also allowed by CDMSlite data, the spin-dependent v^2 and q^2 models (indicated by daggers in Table 1). We finally show the best overall fit, a spin-independent q^4 DM model. However, this model is ruled out by direct detection data by many orders of magnitude. The dark and light blue bands represent the 1 and 2σ errors on modelling, estimated from error propagation of uncertainties in SSM inputs; the green bands represent the 1 and 2σ errors on helioseismological inversions.

frequency separations, assisted by a drop in the base of the convection zone. The former observation tells us that the main improvement comes from better modelling of the region near the solar core. However, the increased tension with measured neutrino fluxes suggests that the decrease in core temperature predicted by models of ADM in the Sun may be too strong. A full DM solution to the solar abundance problem must therefore strike a delicate balance between softer thermal gradients and a lower core temperature.

We end this section by noting that we also provide as supplementary material online a complete table of the boron and beryllium neutrino fluxes, surface helium, radius of the convection zone and small frequency separations for all of our models, in addition to the partial and total chi-squared values defined in Eq. 4.3. This table can be used for quick lookup and interpolation, e.g. for global fits of DM models.

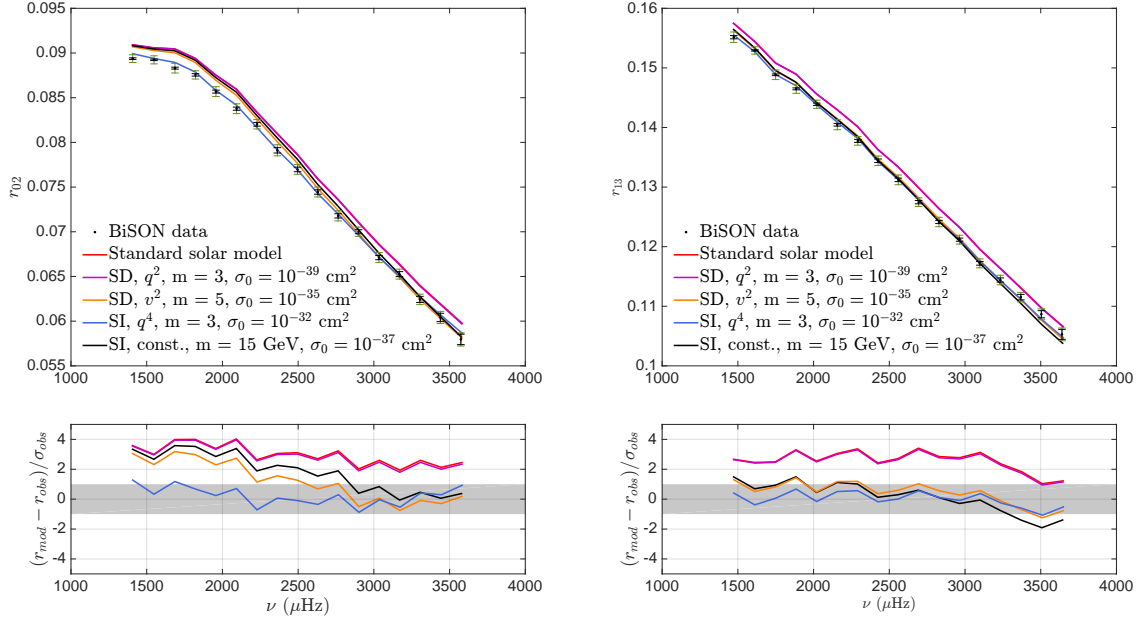


Figure 7. Small frequency separations r_{02} (*left*) and r_{13} (*right*) as defined in Eq. 4.1, for various dark matter models. DM models correspond to the best-fit parameters for two couplings returning the best overall p -values (see Table 1), without being excluded by CDMSlite, along with the best constant case (black), and the overall best fit case (pink). The latter two are however excluded by direct detection. Predictions are compared with helioseismological observations from the BiSON experiment [91]. Inner black error bars correspond to observational error, whereas outer (green) bars also include modelling error. Below each figure we show the residuals with respect to BiSON data, in units of the total error. Though the v^2 model with $m_\chi = 5$ GeV yields substantial improvement in r_{13} for all frequencies, it does less well at low frequencies ($\lesssim 2500$ Hz) with respect to the measured r_{02} .

Table 1. Standard Solar Model (SSM) and best fit (b.f.) values for each of the models we consider, along with observable quantities. Neutrino fluxes are from Ref. [92] while inferred helioseismological quantities are from Ref. [87] and references therein. The DM mass and cross-sections are in GeV and cm^2 , respectively. The ^8B neutrino flux ϕ_{B}^{ν} is in units of $10^{-6} \text{ cm}^{-2} \text{ s}^{-1}$ and the ^7Be neutrino flux ϕ_{Be}^{ν} is expressed in $10^{-9} \text{ cm}^{-2} \text{ s}^{-1}$. The full χ^2 is defined in Eq. 4.3 and includes the neutrino fluxes, surface helium abundance Y_s , depth of the convection zone and small frequency separations. A dagger (\dagger) denotes models that are not ruled out by CDMSlite.

Model	$(m_\chi, \sigma_0)_{b.f.}$	ϕ_{B}^{ν}	ϕ_{Be}^{ν}	R_{CZ}/R_{\odot}	Y_s	χ^2	p	
SSM	–	4.95	4.71	0.722	0.2356	275.9	$< 10^{-10}$	
σ_{SI}	<i>const.</i>	$(15, 10^{-37})$	3.48	4.37	0.721	0.2348	$< 10^{-10}$	
	q^{-2}	$(3, 10^{-36})$	3.9	4.38	0.719	0.2336	0.508	
	q^2	$(3, 10^{-33})$	3.93	4.38	0.719	0.2334	31.02	0.704
	q^4	$(3, 10^{-32})$	3.92	4.36	0.718	0.2331	27.52	0.844
	v^{-2}	$(5, 10^{-34})$	3.82	4.41	0.72	0.2345	75.54	1.26×10^{-4}
	v^2	$(5, 10^{-38})$	3.47	4.28	0.72	0.234	96.48	1.99×10^{-7}
	v^4	$(3, 10^{-37})$	4.31	4.51	0.72	0.2343	85.38	6.84×10^{-6}
σ_{SD}	<i>const.</i>	$(5, 10^{-33})$	3.36	4.27	0.72	0.2341	100.2	5.8×10^{-8}
	q^{-2}	$\dagger (3, 10^{-39})$	3.22	4.16	0.718	0.2333	119.48	$< 10^{-10}$
	q^2	$(5, 10^{-33})$	3.85	4.42	0.721	0.2346	80.7	2.82×10^{-5}
	q^4	$(3, 10^{-31})$	4.69	4.64	0.721	0.2352	194	$< 10^{-10}$
	v^{-2}	$(3, 10^{-31})$	4.11	4.48	0.72	0.2346	82.15	1.83×10^{-5}
	v^2	$\dagger (5, 10^{-35})$	3.88	4.43	0.721	0.2346	83.44	1.24×10^{-5}
	v^4	$\dagger (3, 10^{-37})$	4.39	4.54	0.72	0.2346	110.6	1.63×10^{-9}
Obs.	–	5.00	4.82	0.713	0.2485	–	–	
Obs. error	–	3 %	5%	0.001	0.0034	–	–	
Model error	–	14 %	7%	0.004	0.0035	–	–	

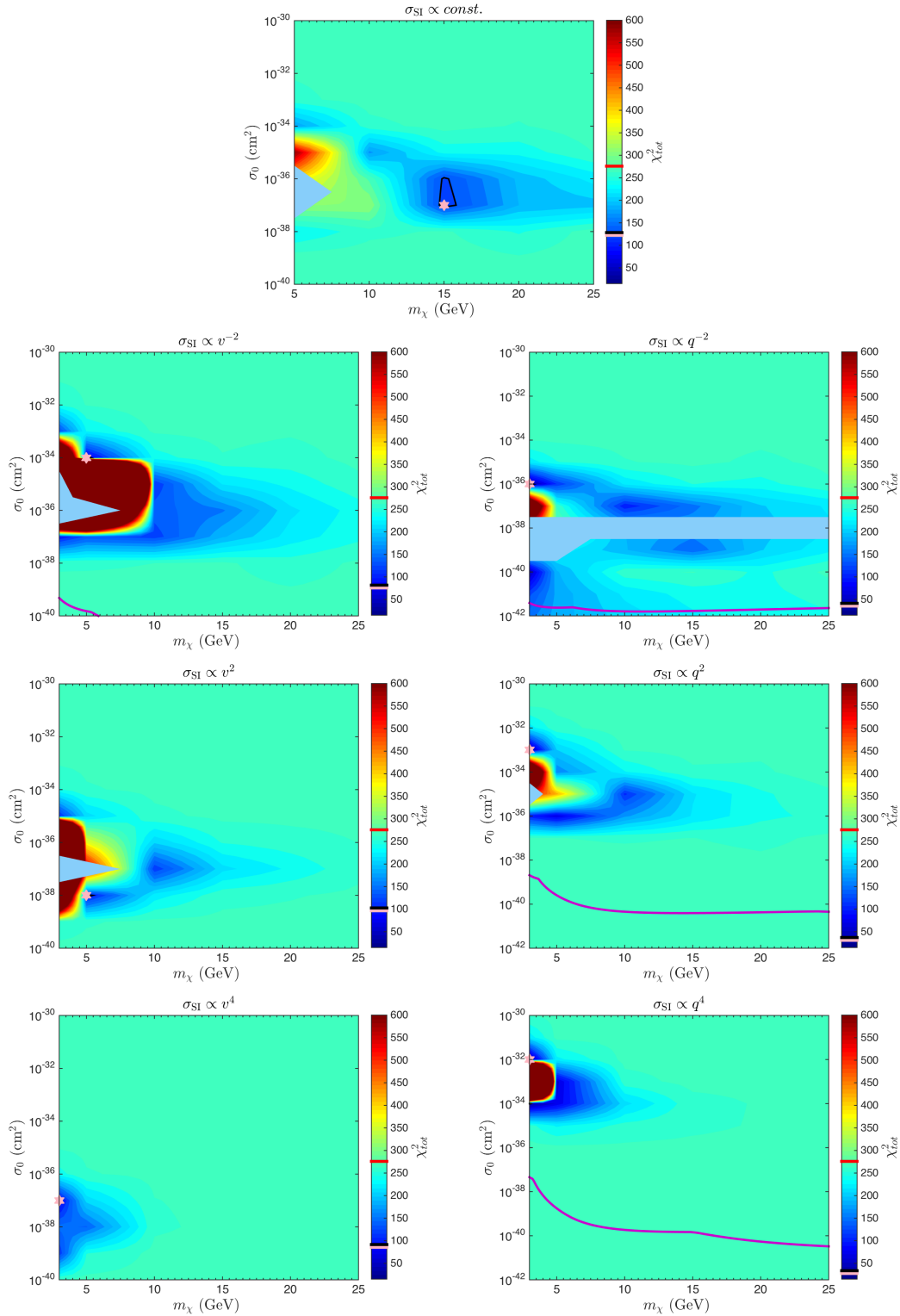


Figure 8. Composite likelihood (Eq. 4.3) including ^8B and ^7Be neutrino flux measurements, surface helium abundance Y_S , depth of the convection zone and small frequency separations. Cross-sections are normalised such that $\sigma = \sigma_0(v/v_0)^{2n}$ or $\sigma = \sigma_0(q/q_0)^{2n}$, with $v_0 = 220 \text{ km s}^{-1}$ and $q_0 = 40 \text{ MeV}$. Best fits are shown as pink stars and pink lines on colour bars. 3σ deviations from the best fits are marked in black, and red lines show the χ^2 value of the SSM. Magenta lines correspond to the CDMSlite 90% upper limits shown in Fig. 5. Panels in which the CDMS line is not seen are completely ruled out. Simulations carried out in the masked regions did not converge, due to the significant heat conduction by the DM particles, leading in extreme cases to density inversions in the core.

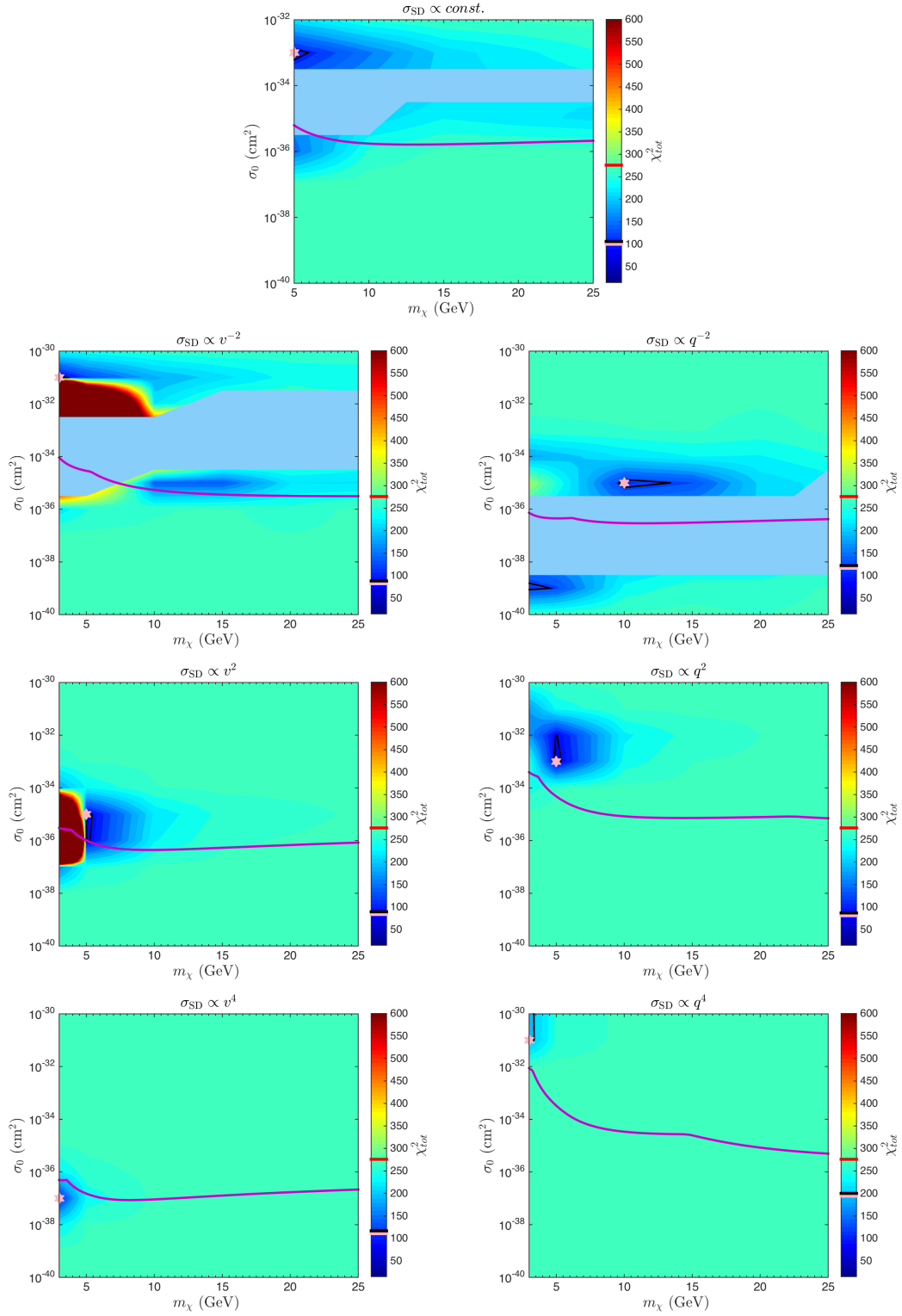


Figure 9. As per Fig. 8, but for spin-dependent couplings.

5 Conclusions

We have presented new limits on momentum and velocity-dependent dark matter from direct detection, and an updated study of their effects on state of the art simulations of the Sun. A correction of the LTE conduction formalism (Eq. 2.12), has shifted the best fits in the parameter space, and the very strong limits from the low-threshold analysis of CDMSlite have ruled out all but a small part of the parameter space of models that can improve the SSM. Our solver could not find solutions for certain values in the parameter space, ostensibly because they led to changes in the solar structure that were too large with respect to the SSM (which it was originally designed to compute). This is not to say that these models are ruled out, however. We note that in some cases (notably spin-dependent v^{-2}), the non-convergence region lies on top of the region that is probed by direct detection. A better exploration of this parameter space could be very interesting indeed.

Of the models that we have found that provide a good fit, only some can be obtained from the current paradigm of simplified models of dark matter. For instance, a spin-dependent v^4 cross section does not occur in such setups. A fermion DM candidate interacting via a vector mediator can give rise to an SD, v^2 cross section, however. This requires a purely vector coupling to the DM, and an axial coupling at the quark level. However, this setup also gives a similar contribution proportional to q^2 (see e.g. [93]), which would be three orders of magnitude larger using our normalisations of q_0 and v_0 , and thus excluded by experiment. This is not to say that this model cannot be obtained, only that it is not straightforward using current tools. A q^{-2} cross section, on the other hand, is closer to a long-range force, which is again not covered in the simplified model approach. A model that can yield a similar type of behaviour would be an electromagnetic dipole or anapole interaction. These models actually couple with mixed powers of v and q , and thus require explicit recalculation of the molecular diffusion and conduction coefficients α and κ , and is the subject of a dedicated study [94].

Finally, we note that the effects of evaporation have not been included here, as the full evaporation formalism must be generalised to the form factor case from scratch. Because the relevant DM masses are so close to the evaporation limit for constant cross-sections ($m_{evap} \sim 4$ GeV), this may have an important impact on the remaining parameter space. Full evaporation rates for momentum- and velocity-dependent interactions will be computed in detail in an upcoming publication [82].

It is clear from the fits we present here that the addition of heat transport by dark matter in the Sun can improve the SSM significantly. The improvement is well beyond what one would naively expect from adding just two degrees of freedom. Even if DM is not the solution, the fact that the true solution can be accurately mimicked by DM would seem to indicate something fundamental about the physical processes behind the solution. Given the types of DM interactions that work, it is clear that if DM *is* to explain the solar composition problem, then a strong model-building effort is required to connect our results with a more robust model of dark matter that can be embedded in a UV-complete theory.

Acknowledgements

We thank Ben Geytenbeek for pointing out the crucial correction to the transported luminosity. ACV thanks Elias Lopez Asamar, David Cerdeño and Ji-Haeng Huh for valuable help with the CDMSlite bounds. We are grateful to the SOM group at IFIC (Universitat de

València – CSIC), for allowing calculations to be performed on SOM2 funded by PROMETEO/2009/116, PROMETEOII/2014/050 and FPA2011-29678. PS is supported by STFC (ST/K00414X/1 and ST/N000838/1) and AS acknowledges support from grants 2014SGR-1458 (Generalitat de Catalunya), ESP2014-56003-R and ESP2015-66134-R (MINECO).

A Contour plots of solar observables

In this appendix we show contour plots for individual quantities impacted by the presence of dark matter in the Sun. In order, we show the boron-8 and beryllium-7 neutrino fluxes, the depth of the convection zone and the goodness of fit (χ^2) computed for the sound speed profile and for the small frequency separations r_{02} and r_{13} .

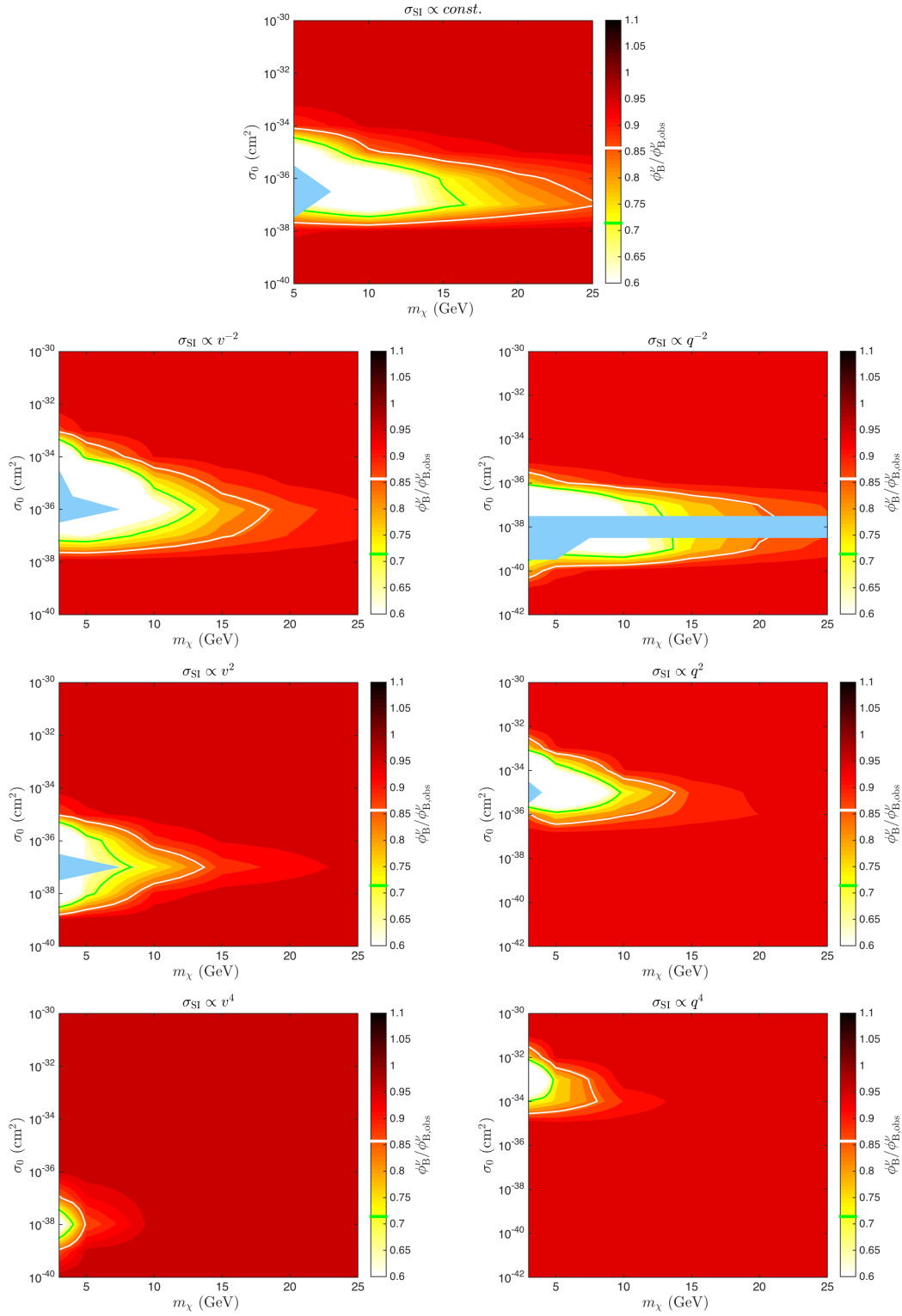


Figure 10. The ratio of the predicted ${}^8\text{B}$ neutrino flux to the measured value $\phi_{\text{B,obs}}^{\nu} = 5.00 \times 10^6 \text{ cm}^{-2}\text{s}^{-1}$ [92], for each type of spin-independent dark matter coupling defined in Eq. 2.1. In every case the white and green lines show the isocontours where the flux is respectively 1 and 2σ lower than the observed values, based on observational (3%) and modelling (14%) errors, added in quadrature. The cross-sections are normalized such that $\sigma = \sigma_0(v/v_0)^{2n}$ or $\sigma = \sigma_0(q/q_0)^{2n}$, with $v_0 = 220 \text{ km s}^{-1}$ and $q_0 = 40 \text{ MeV}$. Simulations carried out in the masked regions did not converge, due to the significant heat conduction by the DM particles, leading in extreme cases to density inversions in the core.

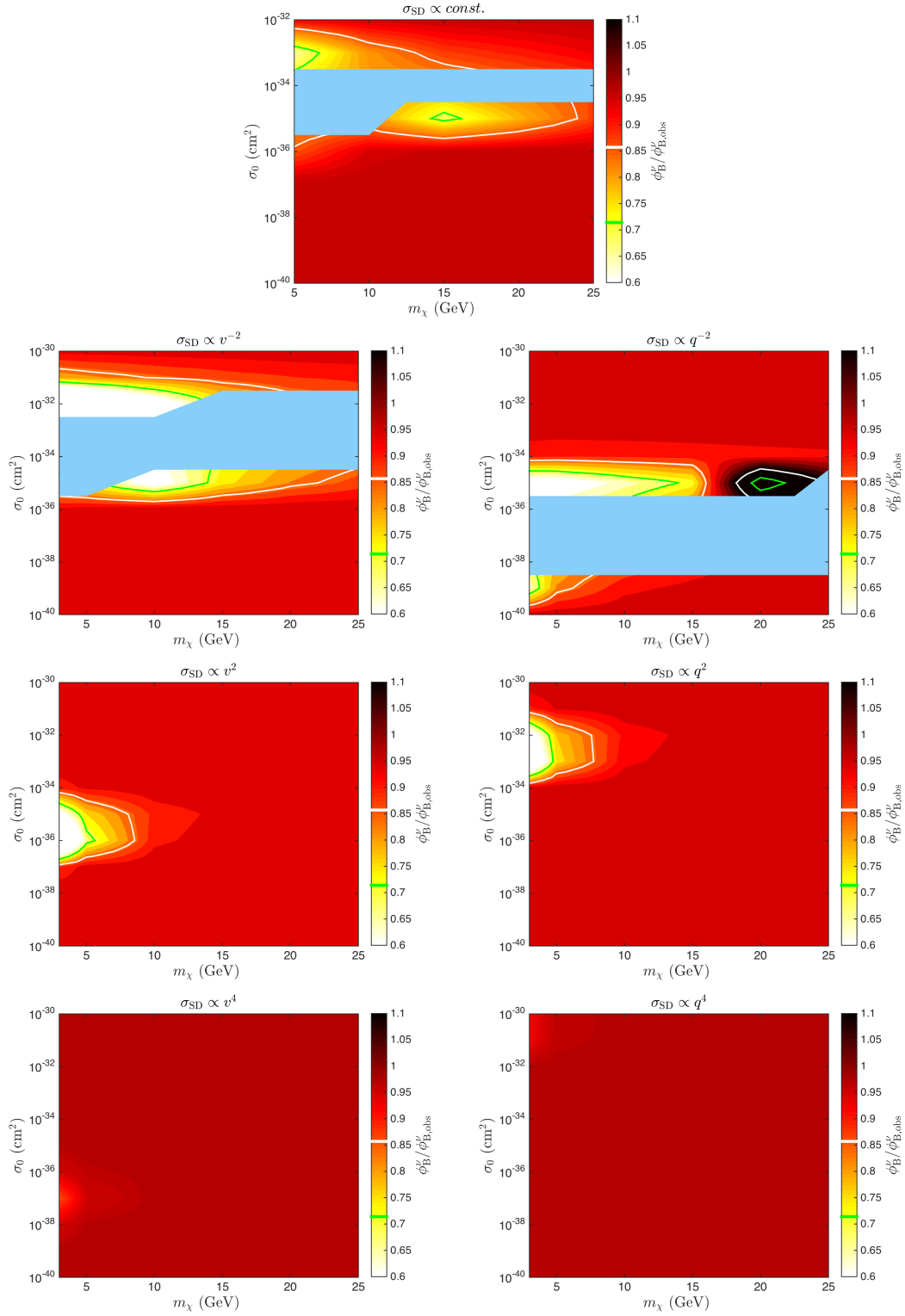


Figure 11. As per Fig. 10, but for spin-dependent couplings.

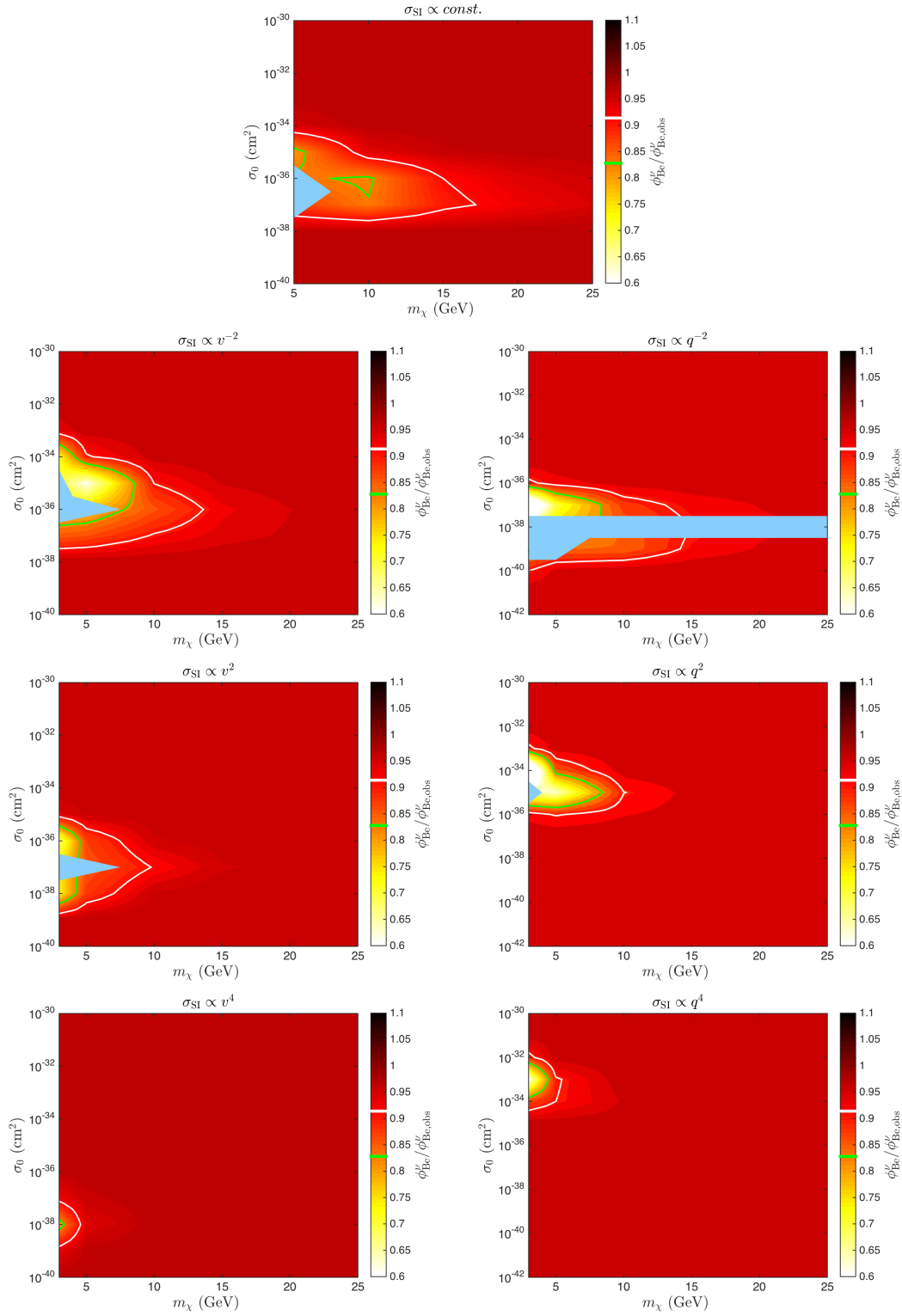


Figure 12. The ratio of the predicted ${}^7\text{Be}$ neutrino flux to the measured value $\phi_{\text{Be,obs}}^\nu = 4.82 \times 10^9 \text{ cm}^{-2}\text{s}^{-1}$ [92], for each type of spin-independent dark matter coupling defined in Eq. 2.1. In every case the white and green lines show the isocontours where the flux is respectively 1 and 2σ lower than the observed values, based on observational (5%) and modelling (7%) errors, added in quadrature. The cross-sections are normalized such that $\sigma = \sigma_0(v/v_0)^{2n}$ or $\sigma = \sigma_0(q/q_0)^{2n}$, with $v_0 = 220 \text{ km s}^{-1}$ and $q_0 = 40 \text{ MeV}$. Regions masked in light blue correspond to parameter combinations where models did not converge.

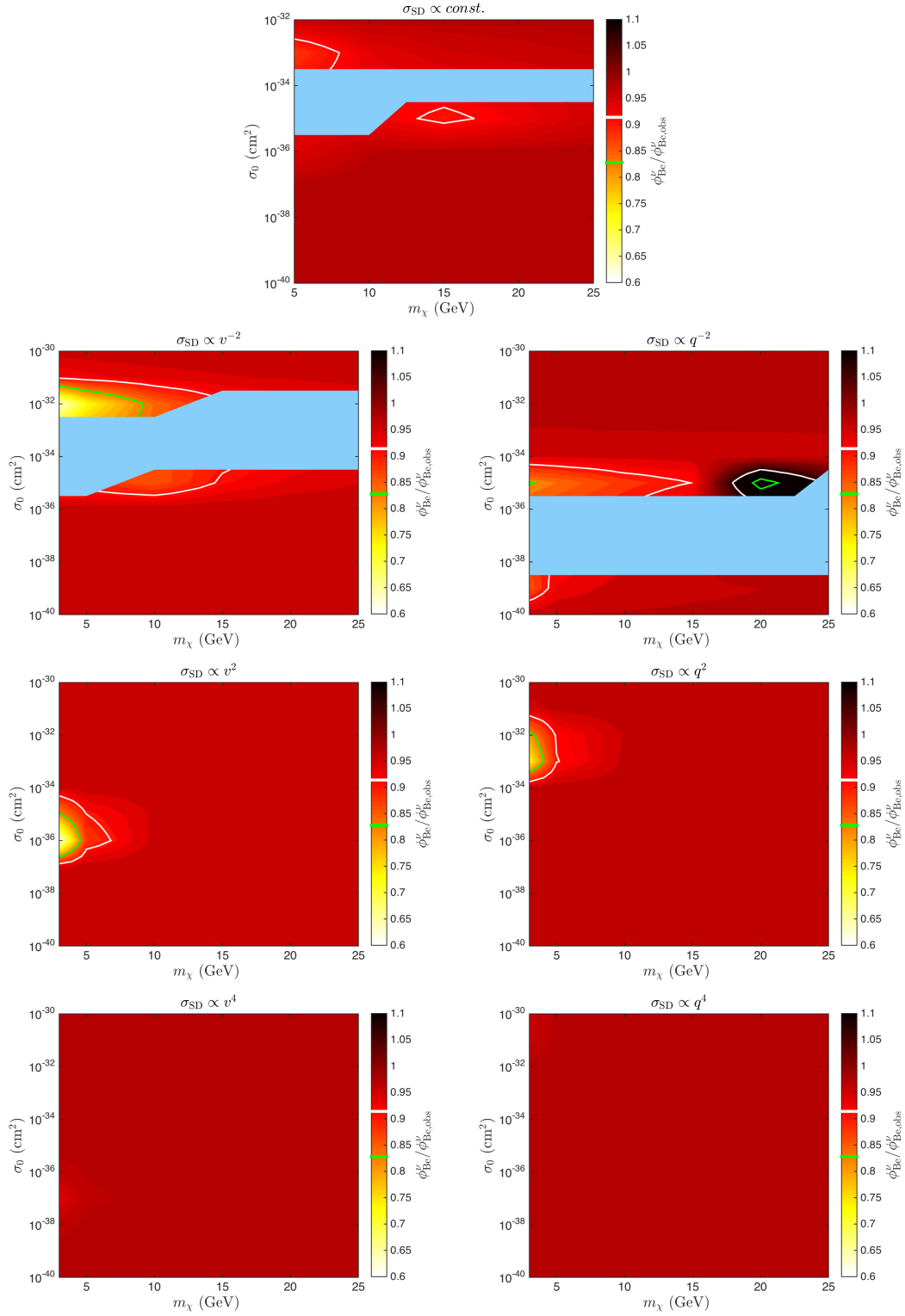


Figure 13. As per Fig. 12, but for spin-dependent couplings.

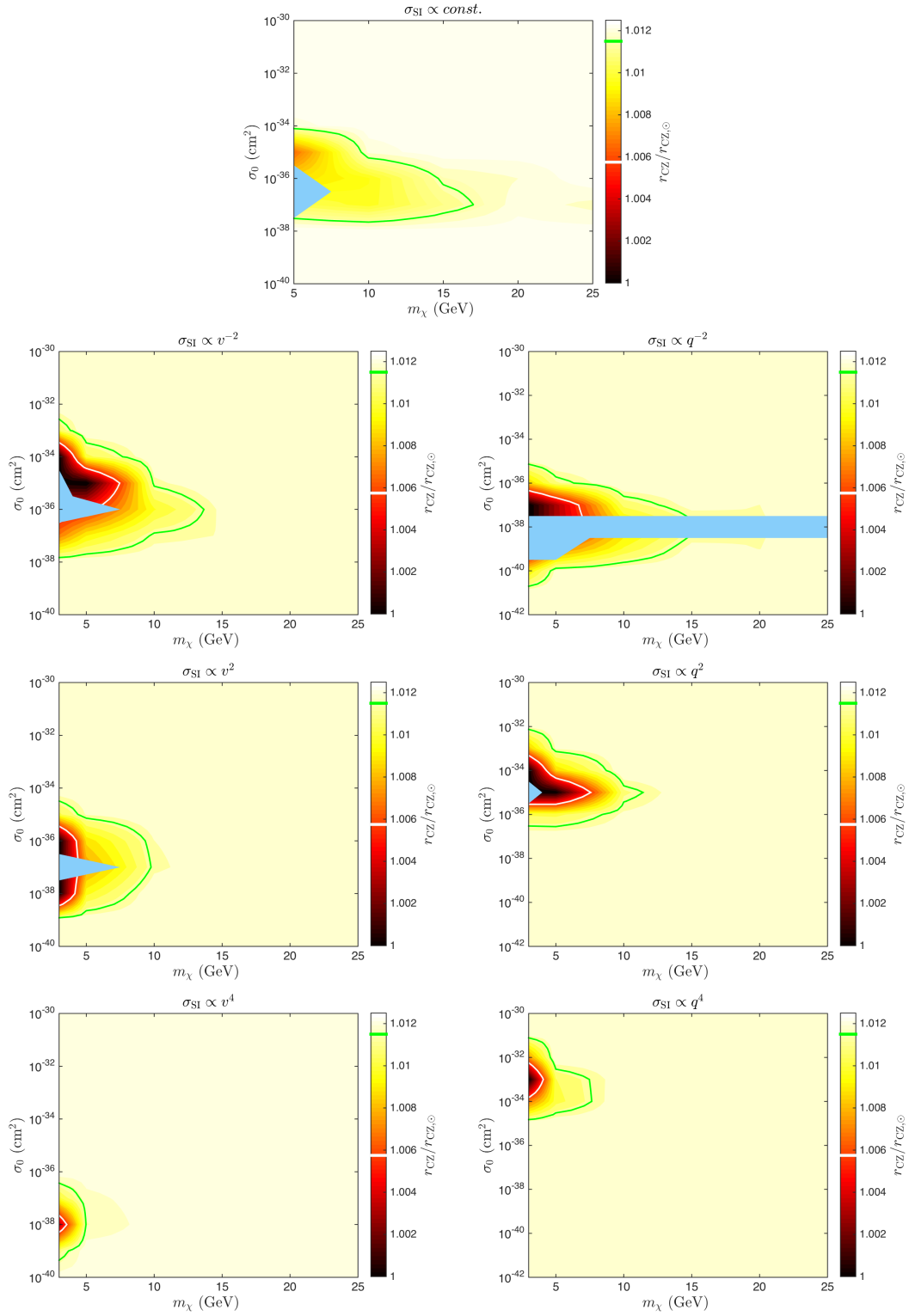


Figure 14. Ratio between the modelled and measured location of the bottom of the convection zone r_{CZ} , for spin-independent couplings. Darker regions represent a better fit to the observed value than the SSM. The white and green lines represent the contours at which the predicted value falls within 1σ and 2σ of the measured value, respectively. The theoretical uncertainty on r_{CZ} ($0.004 R_{\odot}$) is much larger than the experimental error ($0.001 R_{\odot}$), so the former dominates when we add them in quadrature. Regions masked in light blue correspond to parameter combinations where models did not converge.

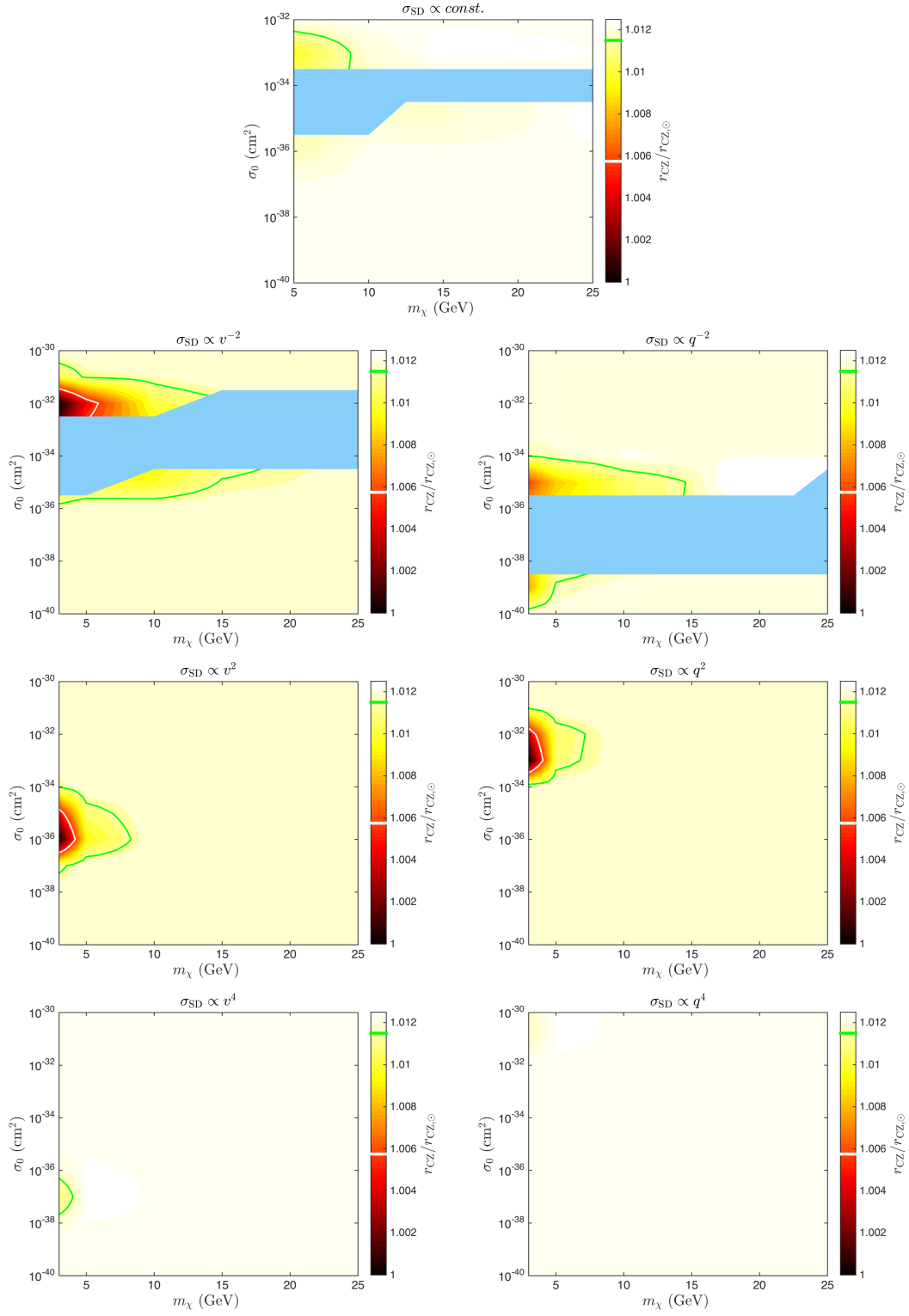


Figure 15. As per Fig. 14, but for spin-dependent couplings.

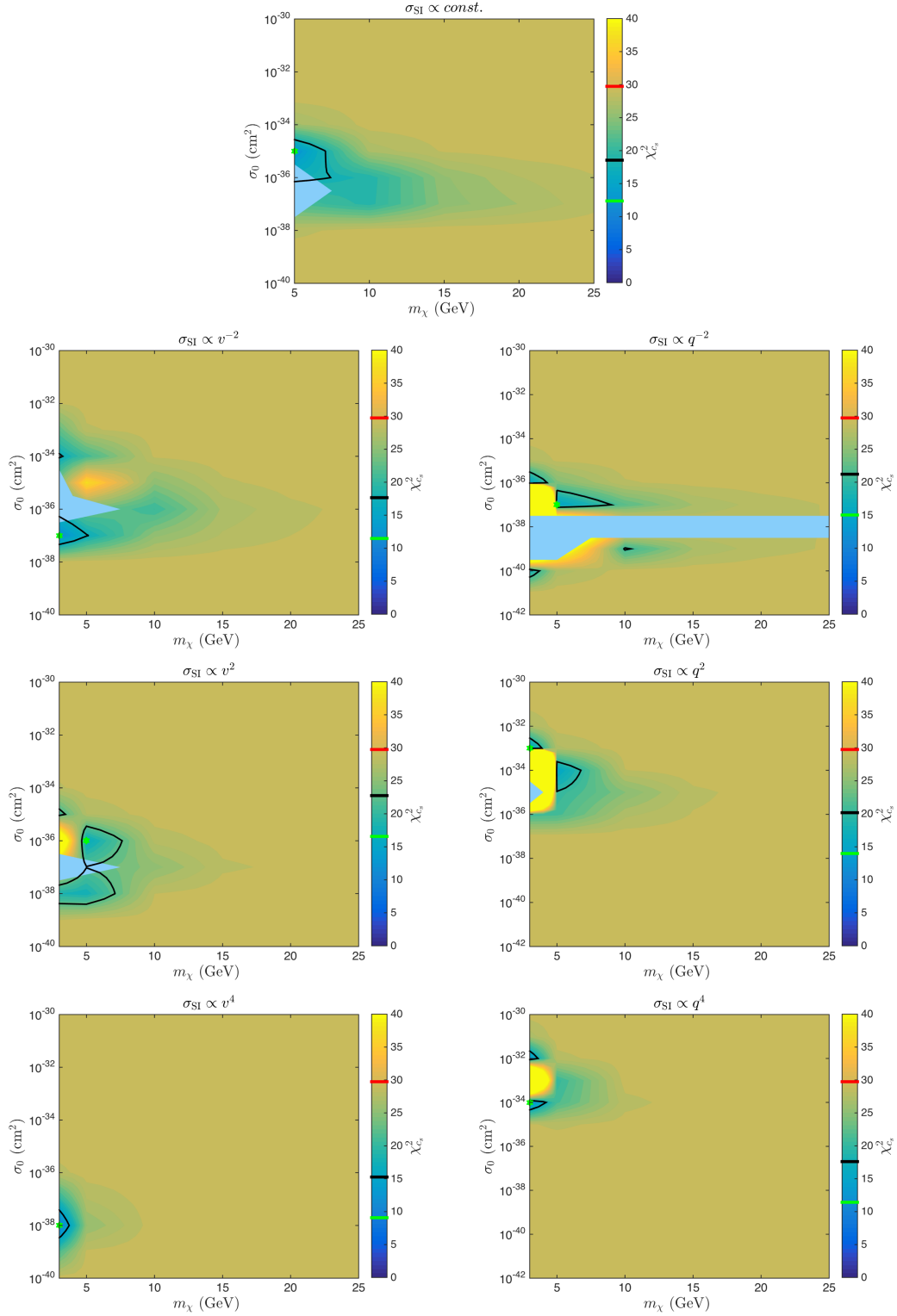


Figure 16. Sound speed χ^2 . Darker regions represent a better fit to the observed value than the SSM. Best fits are shown as green stars and green lines on colour bars. 3σ deviations from the best fits are marked in black, and red lines show the χ^2 value of the SSM. Regions masked in light blue correspond to parameter combinations where models did not converge.

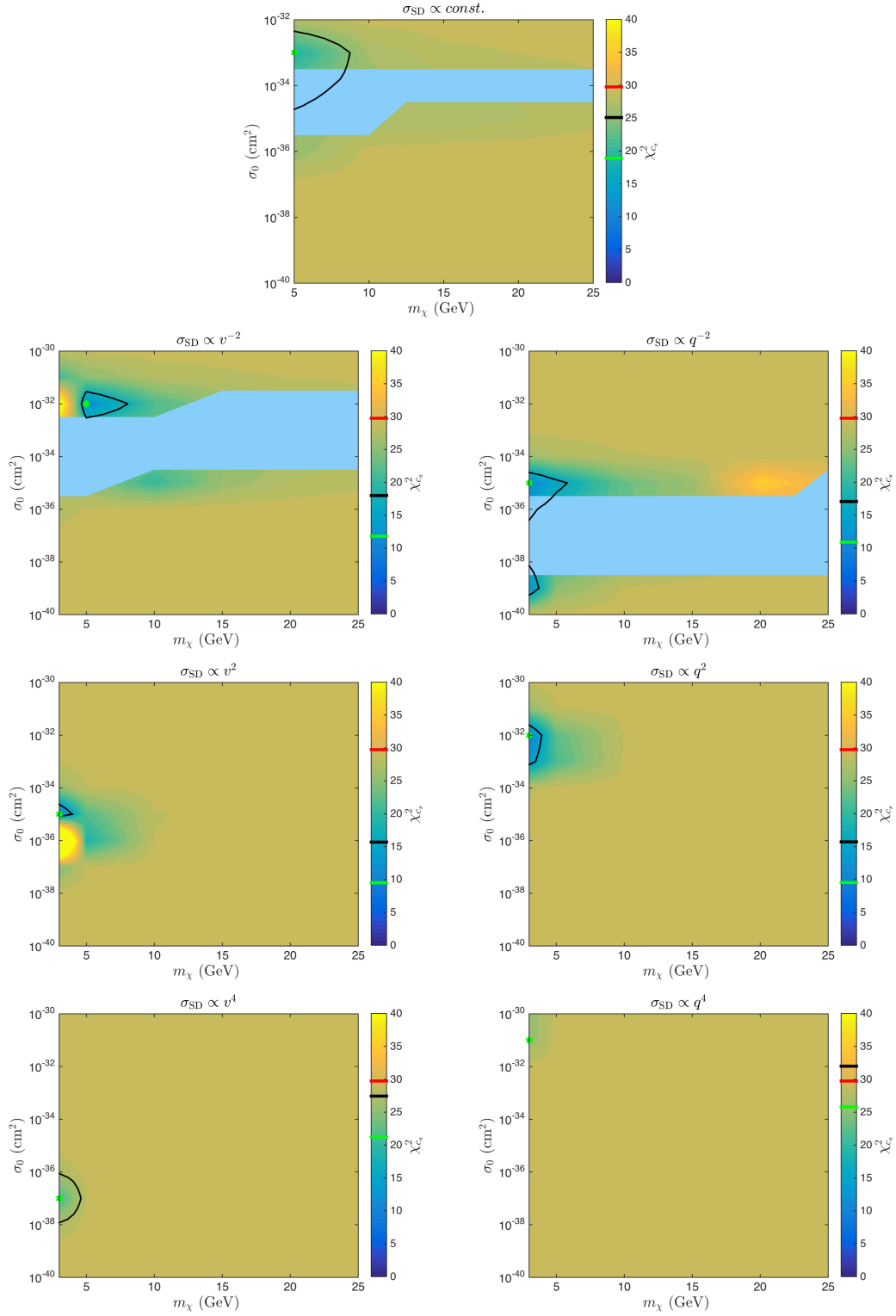


Figure 17. As per Fig. 16, but for spin-dependent couplings.

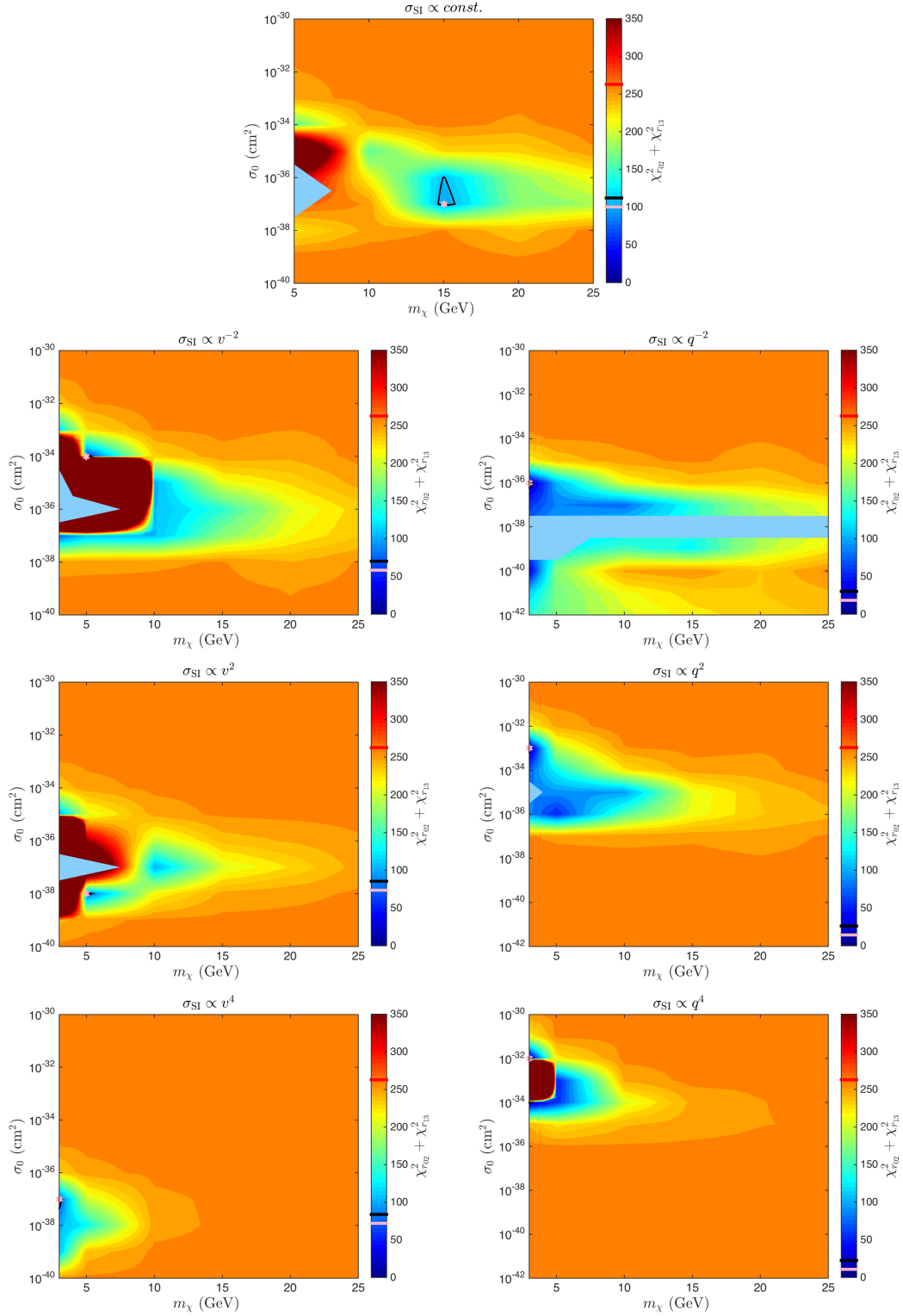


Figure 18. Small frequency separation χ^2 . Blue regions represent a better fit to the observed value than the SSM. Best fits are shown as pink stars and pink lines on colour bars. 3σ deviations from the best fits are marked in black, and red lines show the χ^2 value of the SSM. Regions masked in light blue correspond to parameter combinations where models did not converge.

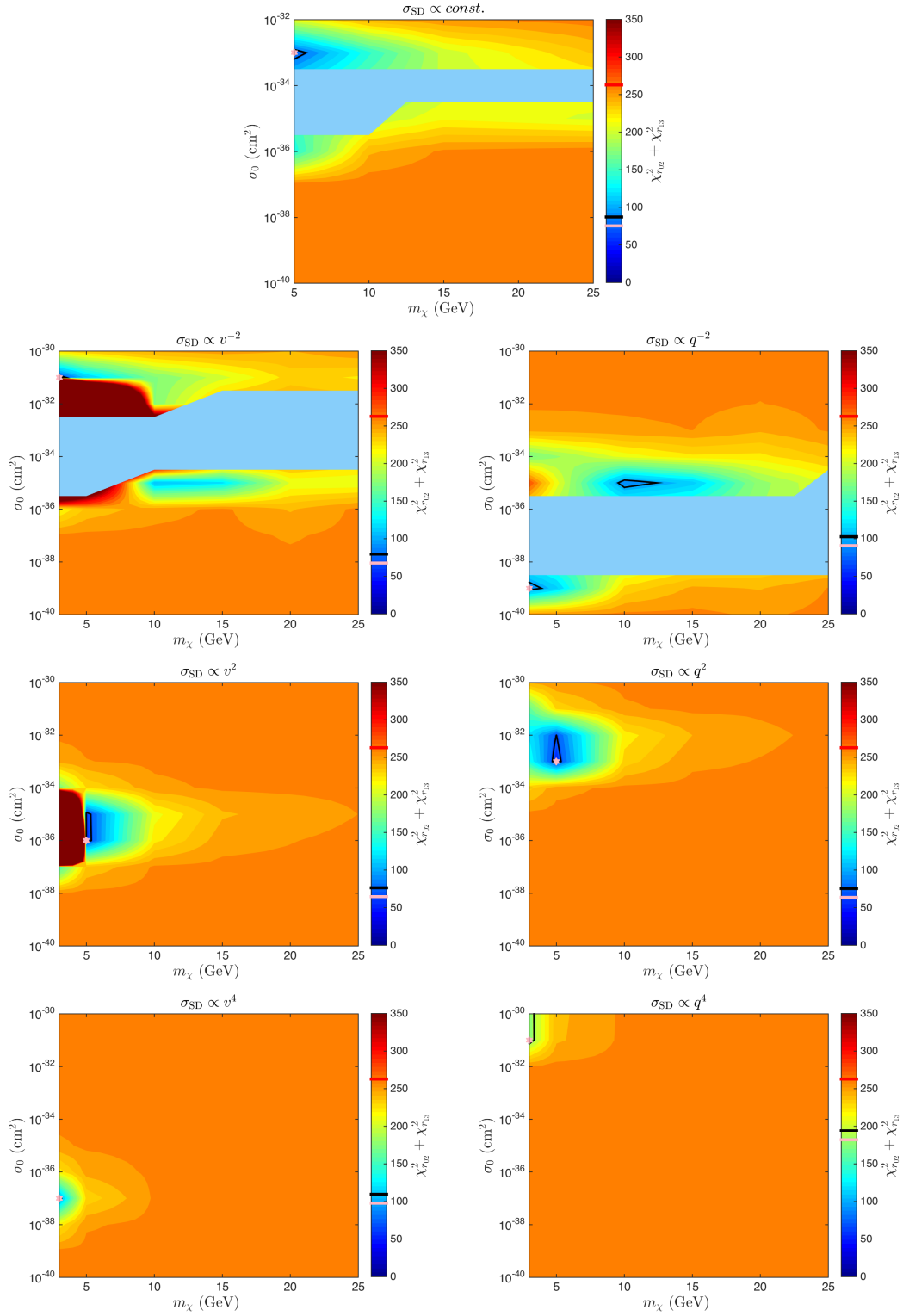


Figure 19. As per Fig. 18, but for spin-dependent couplings.

References

- [1] C. Allende Prieto, D. L. Lambert, and M. Asplund, *The Forbidden Abundance of Oxygen in the Sun*, *ApJ* **556** (2001) L63–L66, [[astro-ph/0106360](#)].
- [2] C. Allende Prieto, D. L. Lambert, and M. Asplund, *A Reappraisal of the Solar Photospheric C/O Ratio*, *ApJ* **573** (2002) L137–L140, [[astro-ph/0206089](#)].
- [3] M. Asplund, N. Grevesse, A. J. Sauval, C. Allende Prieto, and D. Kiselman, *Line formation in solar granulation. IV. [O I], O I and OH lines and the photospheric O abundance*, *A&A* **417** (2004) 751–768, [[astro-ph/0312290](#)].
- [4] M. Asplund, N. Grevesse, A. J. Sauval, C. Allende Prieto, and R. Blomme, *Line formation in solar granulation. VI. [C I], C I, CH and C₂ lines and the photospheric C abundance*, *A&A* **431** (2005) 693–705, [[astro-ph/0410681](#)].
- [5] M. Asplund, N. Grevesse, and A. J. Sauval, *The Solar Chemical Composition*, in *Cosmic Abundances as Records of Stellar Evolution and Nucleosynthesis* (T. G. Barnes III and F. N. Bash, eds.), Astron. Soc. Pac., San Francisco, *ASP Conf. Ser.* **336** (2005) 25.
- [6] P. Scott, M. Asplund, N. Grevesse, and A. J. Sauval, *Line formation in solar granulation. VII. CO lines and the solar C and O isotopic abundances*, *A&A* **456** (2006) 675–688, [[astro-ph/0605116](#)].
- [7] J. Meléndez and M. Asplund, *Another forbidden solar oxygen abundance: the [O I] 5577 Å line*, *A&A* **490** (2008) 817–821, [[arXiv:0808.2796](#)].
- [8] P. Scott, M. Asplund, N. Grevesse, and A. J. Sauval, *On the Solar Nickel and Oxygen Abundances*, *ApJ* **691** (2009) L119–L122, [[arXiv:0811.0815](#)].
- [9] M. Asplund, N. Grevesse, A. J. Sauval, and P. Scott, *The chemical composition of the Sun*, *ARA&A* **47** (2009) 481–522, [[arXiv:0909.0948](#)].
- [10] P. Scott, N. Grevesse, *et. al.*, *The elemental composition of the Sun. I. The intermediate mass elements Na to Ca*, *A&A* **573** (2015) A25, [[arXiv:1405.0279](#)].
- [11] P. Scott, M. Asplund, N. Grevesse, M. Bergemann, and A. J. Sauval, *The elemental composition of the Sun. II. The iron group elements Sc to Ni*, *A&A* **573** (2015) A26, [[arXiv:1405.0287](#)].
- [12] N. Grevesse, P. Scott, M. Asplund, and A. J. Sauval, *The elemental composition of the Sun. III. The heavy elements Cu to Th*, *A&A* **573** (2015) A27, [[arXiv:1405.0288](#)].
- [13] J. N. Bahcall, S. Basu, M. Pinsonneault, and A. M. Serenelli, *Helioseismological implications of recent solar abundance determinations*, *ApJ* **618** (2005) 1049–1056, [[astro-ph/0407060](#)].
- [14] S. Basu and H. Antia, *Constraining solar abundances using helioseismology*, *ApJ* **606** (2004) L85, [[astro-ph/0403485](#)].
- [15] J. N. Bahcall, A. M. Serenelli, and S. Basu, *10,000 Standard Solar Models: A Monte Carlo Simulation*, *ApJS* **165** (2006) 400–431, [[astro-ph/0511337](#)].
- [16] W. M. Yang and S. L. Bi, *Solar Models with Revised Abundances and Opacities*, *ApJ* **658** (2007) L67–L70, [[arXiv:0805.3644](#)].
- [17] S. Basu and H. M. Antia, *Helioseismology and solar abundances*, *Phys. Rep.* **457** (2008) 217–283, [[arXiv:0711.4590](#)].
- [18] A. Serenelli, S. Basu, J. W. Ferguson, and M. Asplund, *New Solar Composition: The Problem With Solar Models Revisited*, *ApJ* **705** (2009) L123–L127, [[arXiv:0909.2668](#)].
- [19] S. Turck-Chieze and I. Lopes, *Toward a unified classical model of the sun: On the sensitivity of neutrinos and helioseismology to the microscopic physics*, *Astrophys. J.* **408** (1993) 347–367.

- [20] J. A. Guzik and K. Mussack, *Exploring mass loss, low-Z accretion, and convective overshoot in solar models to mitigate the solar abundance problem*, *Astrophys. J.* **713** (2010) 1108–1119, [[arXiv:1001.0648](#)].
- [21] J. N. Bahcall, A. M. Serenelli, and S. Basu, *New Solar Opacities, Abundances, Helioseismology, and Neutrino Fluxes*, *ApJ* **621** (2005) L85–L88, [[astro-ph/0412440](#)].
- [22] A. Serenelli, P. Scott, *et. al.*, *Implications of solar wind measurements for solar models and composition*, [arXiv:1604.0531](#).
- [23] M. Lisanti, *Lectures on Dark Matter Physics*, in *Theoretical Advanced Study Institute in Elementary Particle Physics: New Frontiers in Fields and Strings (TASI 2015) Boulder, CO, USA, June 1-26, 2015* (2016) [[arXiv:1603.0379](#)].
- [24] L. M. Krauss, M. Srednicki, and F. Wilczek, *Solar System constraints and signatures for dark-matter candidates*, *Phys. Rev. D* **33** (1986) 2079–2083.
- [25] T. K. Gaisser, G. Steigman, and S. Tilav, *Limits on cold-dark-matter candidates from deep underground detectors*, *Phys. Rev. D* **34** (1986) 2206–2222.
- [26] K. Griest and D. Seckel, *Cosmic asymmetry, neutrinos and the Sun.*, *Nucl. Phys. B* **283** (1987) 681–705.
- [27] R. Gandhi, J. L. Lopez, D. V. Nanopoulos, K.-j. Yuan, and A. Zichichi, *Scrutinizing supergravity models through neutrino telescopes*, *Phys. Rev. D* **49** (1994) 3691–3703, [[astro-ph/9309048](#)].
- [28] A. Bottino, N. Fornengo, G. Mignola, and L. Moscoso, *Signals of neutralino dark matter from earth and sun*, *Astropart. Phys.* **3** (1995) 65–76, [[hep-ph/9408391](#)].
- [29] L. Bergström, J. Edsjö, and P. Gondolo, *Indirect detection of dark matter in km-size neutrino telescopes*, *Phys. Rev. D* **58** (1998) 103519, [[hep-ph/9806293](#)].
- [30] I. P. Lopes and J. Silk, *Solar Neutrinos: Probing the Quasi-isothermal Solar Core Produced by Supersymmetric Dark Matter Particles*, *Physical Review Letters* **88** (2002) 151303, [[astro-ph/0112390](#)].
- [31] I. P. Lopes, J. Silk, and S. H. Hansen, *Helioseismology as a new constraint on supersymmetric dark matter*, *MNRAS* **331** (2002) 361–368, [[astro-ph/0111530](#)].
- [32] V. Barger, F. Halzen, D. Hooper, and C. Kao, *Indirect search for neutralino dark matter with high energy neutrinos*, *Phys. Rev. D* **65** (2002) 075022, [[hep-ph/0105182](#)].
- [33] Super-Kamiokande Collaboration: S. Desai, Y. Ashie, *et. al.*, *Search for dark matter WIMPs using upward through-going muons in Super-Kamiokande*, *Phys. Rev. D* **70** (2004) 083523, [[hep-ex/0404025](#)].
- [34] Super-Kamiokande Collaboration: S. Desai, K. Abe, *et. al.*, *Study of TeV neutrinos with upward showering muons in Super-Kamiokande*, *Astropart. Phys.* **29** (2008) 42–54, [[arXiv:0711.0053](#)].
- [35] IceCube Collaboration: R. Abbasi, Y. Abdou, *et. al.*, *Limits on a Muon Flux from Neutralino Annihilations in the Sun with the IceCube 22-String Detector*, *Phys. Rev. Lett.* **102** (2009) 201302, [[arXiv:0902.2460](#)].
- [36] IceCube Collaboration: R. Abbasi, Y. Abdou, *et. al.*, *Limits on a muon flux from Kaluza-Klein dark matter annihilations in the Sun from the IceCube 22-string detector*, *Phys. Rev. D* **81** (2010) 057101, [[arXiv:0910.4480](#)].
- [37] IceCube Collaboration: R. Abbasi, Y. Abdou, *et. al.*, *Multiyear search for dark matter annihilations in the Sun with the AMANDA-II and IceCube detectors*, *Phys. Rev. D* **85** (2012) 042002, [[arXiv:1112.1840](#)].

- [38] Super-Kamiokande Collaboration: T. Tanaka, K. Abe, *et. al.*, *An Indirect Search for Weakly Interacting Massive Particles in the Sun Using 3109.6 Days of Upward-going Muons in Super-Kamiokande*, *ApJ* **742** (2011) 78, [[arXiv:1108.3384](#)].
- [39] P. Scott, C. Savage, J. Edsjö, and the IceCube Collaboration: R. Abbasi *et al.*, *Use of event-level neutrino telescope data in global fits for theories of new physics*, *JCAP* **11** (2012) 57, [[arXiv:1207.0810](#)].
- [40] H. Silverwood, P. Scott, *et. al.*, *Sensitivity of IceCube-DeepCore to neutralino dark matter in the MSSM-25*, *JCAP* **3** (2013) 27, [[arXiv:1210.0844](#)].
- [41] IceCube Collaboration: M. G. Aartsen, R. Abbasi, *et. al.*, *Search for Dark Matter Annihilations in the Sun with the 79-String IceCube Detector*, *Phys. Rev. Lett.* **110** (2013) 131302, [[arXiv:1212.4097](#)].
- [42] W.-L. Guo, Z.-L. Liang, and Y.-L. Wu, *Direct detection and solar capture of dark matter with momentum and velocity dependent elastic scattering*, *Nucl. Phys. B* **878** (2014) 295–308, [[arXiv:1305.0912](#)].
- [43] R. Catena, *Dark matter signals at neutrino telescopes in effective theories*, *JCAP* **1504** (2015) 052, [[arXiv:1503.0410](#)].
- [44] C. Rott, J. M. Siegal-Gaskins, and J. F. Beacom, *New sensitivity to solar WIMP annihilation using low-energy neutrinos*, *Phys. Rev. D* **88** (2013) 055005, [[arXiv:1208.0827](#)].
- [45] N. Bernal, J. Martn-Albo, and S. Palomares-Ruiz, *A novel way of constraining WIMPs annihilations in the Sun: MeV neutrinos*, *JCAP* **1308** (2013) 011, [[arXiv:1208.0834](#)].
- [46] P. Salati and J. Silk, *A stellar probe of dark matter annihilation in galactic nuclei*, *ApJ* **338** (1989) 24–31.
- [47] A. Bouquet and P. Salati, *Life and death of cosmions in stars*, *A&A* **217** (1989) 270–282.
- [48] I. V. Moskalenko and L. L. Wai, *Dark Matter Burners*, *ApJ* **659** (2007) L29–L32, [[astro-ph/0702654](#)].
- [49] G. Bertone and M. Fairbairn, *Compact stars as dark matter probes*, *Phys. Rev. D* **77** (2008) 043515, [[arXiv:0709.1485](#)].
- [50] D. Spolyar, K. Freese, and P. Gondolo, *Dark Matter and the First Stars: A New Phase of Stellar Evolution*, *Phys. Rev. Lett.* **100** (2008) 051101, [[arXiv:0705.0521](#)].
- [51] M. Fairbairn, P. Scott, and J. Edsjö, *The zero age main sequence of WIMP burners*, *Phys. Rev. D* **77** (2008) 047301, [[arXiv:0710.3396](#)].
- [52] P. Scott, J. Edsjö, and M. Fairbairn, *Low mass stellar evolution with WIMP capture and annihilation*, in *Dark Matter in Astroparticle and Particle Physics: Dark 2007* (H. K. Klapdor-Kleingrothaus and G. F. Lewis, eds.), World Scientific, Singapore (2008) 387–392, [[arXiv:0711.0991](#)].
- [53] F. Iocco, *Dark Matter Capture and Annihilation on the First Stars: Preliminary Estimates*, *ApJ* **677** (2008) L1–L4, [[arXiv:0802.0941](#)].
- [54] F. Iocco, A. Bressan, *et. al.*, *Dark matter annihilation effects on the first stars*, *MNRAS* **390** (2008) 1655–1669, [[arXiv:0805.4016](#)].
- [55] P. Scott, M. Fairbairn, and J. Edsjö, *Dark stars at the Galactic Centre - the main sequence*, *MNRAS* **394** (2009) 82–104, [[0809.1871](#)].
- [56] J. Casanellas and I. Lopes, *The Formation and Evolution of Young Low-mass Stars within Halos with High Concentration of Dark Matter Particles*, *ApJ* **705** (2009) 135–143, [[arXiv:0909.1971](#)].
- [57] E. Ripamonti, F. Iocco, *et. al.*, *First star formation with dark matter annihilation*, *MNRAS* **406** (2010) 2605–2615, [[arXiv:1003.0676](#)].

- [58] E. Zackrisson, P. Scott, *et. al.*, *Finding High-redshift Dark Stars with the James Webb Space Telescope*, *ApJ* **717** (2010) 257–267, [[arXiv:1002.3368](#)].
- [59] E. Zackrisson, P. Scott, *et. al.*, *Observational constraints on supermassive dark stars*, *MNRAS* **407** (2010) L74–L78, [[arXiv:1006.0481](#)].
- [60] P. Scott, A. Venkatesan, *et. al.*, *Impacts of Dark Stars on Reionization and Signatures in the Cosmic Microwave Background*, *ApJ* **742** (2011) 129, [[arXiv:1107.1714](#)].
- [61] I. Lopes and J. Silk, *Solar constraints on asymmetric dark matter*, *Astrophys. J.* **757** (2012) 130, [[arXiv:1209.3631](#)].
- [62] K. Petraki and R. R. Volkas, *Review of Asymmetric Dark Matter*, *Int. J. Mod. Phys. A* **28** (2013) 30028, [[arXiv:1305.4939](#)].
- [63] K. M. Zurek, *Asymmetric Dark Matter: Theories, signatures, and constraints*, *Phys. Rep.* **537** (2014) 91–121, [[arXiv:1308.0338](#)].
- [64] M. Taoso, F. Iocco, G. Meynet, G. Bertone, and P. Eggenberger, *Effect of low mass dark matter particles on the Sun*, *Phys. Rev. D* **82** (2010) 083509, [[arXiv:1005.5711](#)].
- [65] D. T. Cumberbatch, J. Guzik, J. Silk, L. S. Watson, and S. M. West, *Light WIMPs in the Sun: Constraints from Helioseismology*, *Phys. Rev. D* **82** (2010) 103503, [[arXiv:1005.5102](#)].
- [66] I. Lopes and J. Silk, *Solar Constraints on Asymmetric Dark Matter*, *ApJ* **757** (2012) 130, [[arXiv:1209.3631](#)].
- [67] A. C. Vincent and P. Scott, *Thermal conduction by dark matter with velocity and momentum-dependent cross-sections*, *JCAP* **4** (2014) 19, [[arXiv:1311.2074](#)].
- [68] I. Lopes, K. Kadota, and J. Silk, *Constraint on Light Dipole Dark Matter from Helioseismology*, *ApJ* **780** (2014) L15, [[arXiv:1310.0673](#)].
- [69] I. Lopes, P. Panci, and J. Silk, *Helioseismology with Long-range Dark Matter-Baryon Interactions*, *ApJ* **795** (2014) 162, [[arXiv:1402.0682](#)].
- [70] A. C. Vincent, P. Scott, and A. Serenelli, *Possible Indication of Momentum-Dependent Asymmetric Dark Matter in the Sun*, *Phys. Rev. Lett.* **114** (2015) 081302, [[arXiv:1411.6626](#)].
- [71] A. C. Vincent, A. Serenelli, and P. Scott, *Generalised form factor dark matter in the Sun*, *JCAP* **1508** (2015) 040, [[arXiv:1504.0437](#)].
- [72] J. Fan, M. Reece, and L.-T. Wang, *Non-relativistic effective theory of dark matter direct detection*, *Journal of Cosmology and Astroparticle Physics* **2010** (2010) 042.
- [73] P. Panci, *New Directions in Direct Dark Matter Searches*, *Adv. High Energy Phys.* **2014** (2014) 681312, [[arXiv:1402.1507](#)].
- [74] G. Angloher *et. al.*, *Limits on momentum-dependent asymmetric dark matter with CRESST-II*, [[arXiv:1601.0444](#)].
- [75] SuperCDMS: R. Agnese *et. al.*, *New Results from the Search for Low-Mass Weakly Interacting Massive Particles with the CDMS Low Ionization Threshold Experiment*, *Phys. Rev. Lett.* **116** (2016) 071301, [[arXiv:1509.0244](#)].
- [76] B. Feldstein, A. L. Fitzpatrick, and E. Katz, *Form Factor Dark Matter*, *JCAP* **1001** (2010) 020, [[arXiv:0908.2991](#)].
- [77] J. Fan, M. Reece, and L.-T. Wang, *Non-relativistic effective theory of dark matter direct detection*, *JCAP* **1011** (2010) 042, [[arXiv:1008.1591](#)].
- [78] J. Kumar and D. Marfatia, *Matrix element analyses of dark matter scattering and annihilation*, *Phys. Rev.* **D88** (2013) 014035, [[arXiv:1305.1611](#)].
- [79] A. L. Fitzpatrick, W. Haxton, E. Katz, N. Lubbers, and Y. Xu, *The effective field theory of dark matter direct detection*, *JCAP* **2** (2013) 4, [[arXiv:1203.3542](#)].

- [80] R. Catena and B. Schwabe, *Form factors for dark matter capture by the Sun in effective theories*, *JCAP* **1504** (2015) 042, [[arXiv:1501.0372](#)].
- [81] R. H. Helm, *Inelastic and Elastic Scattering of 187-Mev Electrons from Selected Even-Even Nuclei*, *Phys. Rev.* **104** (1956) 1466–1475.
- [82] G. Busoni *et. al.* *In preparation* (2016).
- [83] A. Gould and G. Raffelt, *Thermal conduction by massive particles*, *ApJ* **352** (1990) 654–668.
- [84] A. Bottino, G. Fiorentini, *et. al.*, *Does solar physics provide constraints to weakly interacting massive particles?*, *Phys. Rev. D* **66** (2002) 053005, [[hep-ph/0206211](#)].
- [85] P. Klos, J. Menendez, D. Gazit, and A. Schwenk, *Large-scale nuclear structure calculations for spin-dependent WIMP scattering with chiral effective field theory currents*, *Phys. Rev.* **D88** (2013) 083516, [[arXiv:1304.7684](#)]. [Erratum: *Phys. Rev.*D89,no.2,029901(2014)].
- [86] A. Weiss and H. Schlattl, *GARSTEC: the Garching Stellar Evolution Code. The direct descendant of the legendary Kippenhahn code*, *Ap&SS* **316** (2008) 99–106.
- [87] A. M. Serenelli, W. C. Haxton, and C. Peña-Garay, *Solar Models with Accretion. I. Application to the Solar Abundance Problem*, *ApJ* **743** (2011) 24, [[arXiv:1104.1639](#)].
- [88] P. Scott, J. Edsjö, and M. Fairbairn, *The DarkStars code: a publicly available dark stellar evolution package*, in *Dark 2009* (H. V. Klapdor-Kleingrothaus & I. V. Krivosheina, ed.), World Scientific (2010) 320–327, [[arXiv:0904.2395](#)].
- [89] S. Basu, W. J. Chaplin, Y. Elsworth, R. New, and A. M. Serenelli, *Fresh Insights on the Structure of the Solar Core*, *ApJ* **699** (2009) 1403–1417, [[arXiv:0905.0651](#)].
- [90] I. W. Roxburgh and S. V. Vorontsov, *The ratio of small to large separations of acoustic oscillations as a diagnostic of the interior of solar-like stars*, *A&A* **411** (2003) 215–220.
- [91] S. Basu, W. J. Chaplin, *et. al.*, *Solar abundances and helioseismology: Fine structure spacings and separation ratios of low-degree p modes*, *ApJ* **655** (2007) 660–671, [[astro-ph/0610052](#)].
- [92] Super-Kamiokande: K. Abe *et. al.*, *Solar neutrino results in Super-Kamiokande-III*, *Phys. Rev.* **D83** (2011) 052010, [[arXiv:1010.0118](#)].
- [93] J. B. Dent, L. M. Krauss, J. L. Newstead, and S. Sabharwal, *General analysis of direct dark matter detection: From microphysics to observational signatures*, *Phys. Rev.* **D92** (2015) 063515, [[arXiv:1505.0311](#)].
- [94] B. Geytenbeek, S. Roa, *et. al.*, *Effect of electromagnetic dipole dark matter on energy transport in the solar interior*, [arXiv:1610.0673](#).